



# **Drivers of permafrost degradation along the Inuvik to Tuktoyaktuk Highway (ITH)**

Master's thesis in Remote Sensing, geoinformation and Visualisation

by  
**JENNIKA HAMMAR**

Supervisors

**Prof. Dr. Guido Grosse**

University of Potsdam

Alfred Wegener Institute for Polar and Marine Research, Potsdam

**Dr. Inge Grünberg**

Alfred Wegener Institute for Polar and Marine Research, Potsdam

Institute of Geosciences

UNIVERSITY OF POTSDAM

Potsdam, Germany 24 February 2022

# Abstract

Infrastructure construction on permafrost is challenging. Not only are northern regions undergoing a faster and more intense global warming than the rest of the world, inducing thawing of the permafrost at a worldwide scale. In addition, linear infrastructures such as gravel highways, built on embankments to protect the underlying permafrost, change environmental conditions in various ways, enhancing permafrost degradation. This work aims to utilize remote sensing data and explore the physical parameters that drive permafrost degradation in the regions adjacent to the Inuvik to Tuktoyaktuk Highway (ITH) in Northwest Territories, Canada. Within the work, snow accumulation along the embankment toe, vegetation moisture increase, surface water increase in poorly drained areas, earlier snowmelt and vegetation increase along the road are defined as factors that (I) enhance permafrost degradation and (II) are observable using remote sensing techniques. The analysis is conducted using cloud computing services, open-source software packages, and primarily freely available datasets. Snow accumulation conditions are derived using Digital Elevation Models (DEM) as baseline data. The cardinal direction of the road and the predominating wind direction significantly impact the snow accumulation. Moreover, the results indicate that the enhanced snow accumulation generally reaches further distances from the road than previous studies suggest. The impact from the road on vegetation moisture and vegetation conditions, indicated by the Normalized Difference Moisture Index (NDMI) and the Normalized Difference Vegetation Index (NDVI), respectively, demonstrated significant decreases within the first 25 m from the road edge. This is in line with previous studies. However, whether the observed effect reflects the field conditions or if the spectral signal is affected by other factors like dust is critically discussed. Furthermore, my study revealed that by normalizing the median NDMI and NDVI values on an undisturbed reference area, an addi-

---

tional effect is observed reaching up to 200 m from the road. The analysis of the NIR band indicates that the downstream side became wetter throughout the years compared to the upstream side. The snowmelt pattern indicated by the Normalized Difference Snow Index (NDSI), derived from Landsat images, shows that the areas next to the road are snow-free earlier in spring than the areas further away. The result indicates that the road affects the snowmelt up to 600 m from the road. The findings of this work highlight the importance of future research into the impact of dust on satellite-derived indices. Furthermore, the findings contribute to a better understanding of the spatial scale of altered permafrost drivers following the construction of the ITH.

**Keywords:** Canada; arctic highways; permafrost degradation; snow accumulation; airborne laser scanner; remote sensing indices; Sentinel-2; Landsat

## Abstract (German)

Der Bau von Infrastrukturen auf Permafrostböden ist eine Herausforderung. Nicht nur, dass die nördlichen Regionen einer schnelleren und intensiveren globalen Erwärmung ausgesetzt sind als der Rest der Welt, was zu einem weltweiten Auftauen des Permafrosts führt. Darüber hinaus verändern lineare Infrastrukturen wie Schotterstraßen, die auf Dämmen gebaut werden, um den darunter liegenden Permafrost zu schützen, die Umweltbedingungen auf verschiedene Weise und verstärken den Abbau des Permafrosts. Diese Arbeit zielt darauf ab, Fernerkundungsdaten zu nutzen, und die physikalischen Parameter zu erforschen, die die Permafrostdegradation in den an den Inuvik to Tuktoyaktuk Highway (ITH) angrenzenden Regionen in den kanadischen Northwest-Territorien vorantreiben. Im Rahmen der Arbeit werden die Schneeakkumulation entlang der Böschungsspitzen, die Feuchtigkeit der Vegetation, die Zunahme des Oberflächenwassers in schlecht entwässerten Gebieten, die frühere Schneeschmelze und die Zunahme der Vegetation entlang der Straße als Faktoren definiert, die (I) die Permafrostdegradation verstärken und (II) mit Fernerkundungstechniken beobachtet werden können. Die Analyse wird mithilfe von Cloud-Computing-Diensten, Open-Source-Softwarepaketen und hauptsächlich frei verfügbaren Datensätzen durchgeführt. Die Schneeakkumulationsbedingungen werden mithilfe von digitalen Höhenmodellen (DEM) als Basisdaten abgeleitet. Die Himmelsrichtung der Straße und die vorherrschende Windrichtung haben einen erheblichen Einfluss auf die Schneeakkumulation. Außerdem zeigen die Ergebnisse, dass die verstärkte Schneeakkumulation im Allgemeinen weiter von der Straße entfernt ist, als frühere Studien vermuten ließen. Die Auswirkungen der Straße auf die Vegetationsfeuchtigkeit und den Vegetationszustand, die durch den Normalized Difference Moisture Index (NDMI) bzw. den Normalized Difference Vegetation Index (NDVI) angezeigt werden, zeigten eine signifikante Abnahme innerhalb der ersten 25 m vom

---

Straßenrand. Dies steht im Einklang mit früheren Studien. Es wird jedoch kritisch diskutiert, ob der beobachtete Effekt die Feldbedingungen widerspiegelt, oder ob das spektrale Signal durch andere Faktoren wie zum Beispiel Staub beeinflusst wird. Darüber hinaus ergab meine Studie, dass durch die Normalisierung der mittleren NDMI- und NDVI-Werte auf eine ungestörte Referenzfläche ein zusätzlicher Effekt zu erkennen war, der bis zu einer Entfernung von 200 m von der Straße reichte. Die Analyse des NIR-Bandes zeigt, dass die flussabwärts gelegene Seite im Vergleich zur flussaufwärts gelegenen Seite im Laufe der Jahre feuchter wurde.

Das Schneeschmelzmuster, das durch den aus Landsat-Bildern abgeleiteten Normalized Difference Snow Index (NDSI) angezeigt wird, lässt erkennen, dass die Gebiete in Straßennähe im Frühjahr früher schneefrei sind als die weiter entfernten Gebiete. Das Ergebnis zeigt, dass die Straße die Schneeschmelze bis zu einer Entfernung von 600 m von der Straße beeinflusst. Die Ergebnisse dieser Arbeit machen deutlich, wie wichtig künftige Forschungen über die Auswirkungen von Staub auf satellitengestützte Indizes sind. Darüber hinaus tragen die Ergebnisse zu einem besseren Verständnis des räumlichen Ausmaßes der veränderten Permafrosttreiber nach dem Bau der ITH bei.

**Schlüsselwörter:** Kanada; arktische Straßen; Permafrostdegradation; Schneeakkumulation; Airborne Laserscanner; Fernerkundungsindizes; Sentinel-2; Landsat

## Acknowledgements

First, I want to thank Dr. Inge Grünberg for her excellent supervision throughout the thesis, great scientific support, her many ideas, invaluable comments on my writing and the thesis structure. I want to express my gratitude to Prof. Dr. Guido Grosse for allowing me to complete this thesis under his supervision and giving me the freedom to pursue my ideas. I thank Prof. Dr. Julia Boike for giving me the opportunity of conducting this research and for all the scientific support and personal encouragement. I want to thank AWI for providing me with the opportunity to get experience in a scientific setting outside of the university. A special thanks go to my friends, fellow students and flatmates, who put up with my mood swings during this time and were able to motivate me again and again. Finally, I am deeply grateful to my parents for their unconditional support.

Jennika Hammar, Berlin, February 2022



# Contents

<b>List of Figures</b>	<b>viii</b>
<b>List of Tables</b>	<b>x</b>
<b>1 Introduction</b>	<b>1</b>
<b>2 Datasets &amp; Methods</b>	<b>5</b>
2.1 Study Area . . . . .	5
2.2 Airborne Laser Scanner Data . . . . .	9
2.3 Sentinel-2 . . . . .	10
2.3.1 Initial Filtering . . . . .	12
2.3.2 Atmospheric Correction . . . . .	13
2.3.3 Cloud Masking . . . . .	15
2.3.4 Indices . . . . .	16
2.3.5 Co-registration . . . . .	19
2.3.6 Pixel-based Analysis . . . . .	19
2.3.7 Landsat . . . . .	22
<b>3 Results</b>	<b>26</b>
3.1 Snow Accumulation . . . . .	26
3.2 Vegetation Moisture Content and Surface Water . . . . .	32
3.3 Snow Melt . . . . .	35
3.4 Vegetation Greenness . . . . .	36
<b>4 Discussion</b>	<b>39</b>
4.1 Snow Accumulation . . . . .	39
4.2 Vegetation Moisture Content and Surface Water . . . . .	42



4.3	Snow Melt . . . . .	44
4.4	Vegetation Greenness . . . . .	46
<b>5</b>	<b>Conclusion</b>	<b>49</b>
	<b>Bibliography</b>	<b>51</b>

# List of Figures

2.1	Study area. . . . .	6
2.2	Profile elevation of ITH. . . . .	7
2.3	Monthly mean air temperature in Inuvik (2016–2020). . . . .	8
2.4	Processing steps for the Sentinel-2 data. . . . .	12
2.5	Number of utilized Sentinel-2 images. . . . .	13
2.6	TOA and BOA reflectance . . . . .	14
2.7	Cloud masking . . . . .	16
2.8	Bandwidths and names for Landsat-7, -8 and Sentinel-2 . . . . .	16
2.9	Images of water body in true colors, NDWI and NIR . . . . .	18
2.10	Buffer zones around the road. . . . .	21
2.11	Development of a water pond in the vicinity of the road. . . . .	21
2.12	Method for NIR band pixel selection . . . . .	22
2.13	Process chain for snow discrimination . . . . .	24
2.14	True color and NDSI example from Landsat-8 . . . . .	25
3.1	Snow depths. . . . .	27
3.2	Elevation transects with and without snow. . . . .	29
3.3	Snow accumulation in north-south direction . . . . .	30
3.4	Snow accumulation in east-west direction . . . . .	31
3.5	Temporal and spatial changes in NDMI with distance from the road edge. . . . .	33
3.6	Distribution of NIR reflectance upstream and downstream. . . . .	35
3.7	Presence of snow with distance from ITH . . . . .	36
3.8	Distribution of NDVI with distance from the road edge. . . . .	37
3.9	Maximum NDVI for a road segment in 2016 and 2020. . . . .	38

4.1 Wind rose for Trail Valley Creek. . . . . 41

4.2 Photos of the ITH and the adjacent vegetation. . . . . 47

# List of Tables

2.1	The spectral region, wavelength range and spatial resolution of each Sentinel-2 band. . . . .	11
2.2	The spectral region, wavelength range and spatial resolution for each Landsat-8 OLI satellite band. . . . .	23

# Abbreviations and Symbols

$\theta$	Solar zenith angle in radians
$\rho$	Surface reflectance
$\tau$	Transmissivity
$d$	Earth-Sun distance
$E_{dif}$	Diffuse solar irradiance
$E_{dir}$	Direct solar irradiance
$ESUN(\lambda)$	Solar exoatmospheric spectral irradiance corrected for daily variations
$L_p$	Path radiance
$L_{TOA}$	TOA radiance
$R_{TOA}$	TOA reflectance
<b>ALS</b>	Airborne Laser Scanner
<b>API</b>	Application programming interface
<b>AROSICS</b>	Automated and Robust Open-Source Image Co-Registration Software
<b>AWI</b>	Alfred Wegener Institute
<b>BOA</b>	Bottom of Atmosphere
<b>DEM</b>	Digital Elevation Model
<b>DTM</b>	Digital Terrain Model
<b>ETM</b>	Enhanced Thematic Mapper
<b>GDAL</b>	Geospatial Data Abstraction Library

<b>GEE</b>	Google Earth Engine
<b>IDE</b>	Interactive development environment
<b>IQR</b>	Interquartile range
<b>ITH</b>	Inuvik to Tuktoyaktuk Highway
<b>MGRS</b>	Military Grid Reference System
<b>MSI</b>	Multispectral Instrument
<b>NDMI</b>	Normalized Difference Moisture Index
<b>NDSI</b>	Normalized Difference Snow Index
<b>NDWI</b>	Normalized Difference Water Index
<b>NDVI</b>	Normalized Difference Vegetation Index
<b>NIR</b>	Near-infrared
<b>OLI</b>	Operational Land Imager
<b>UAV</b>	Unmanned Aerial Vehicle
<b>USGS</b>	United States Geological Survey
<b>SPOT</b>	Satellite pour l'Observation de la Terre
<b>6S</b>	Second Simulation of the Satellite Signal in the Solar Spectrum
<b>SLC</b>	Scan Line Corrector
<b>SfM</b>	Structure from Motion
<b>SWIR</b>	Short-wave-infrared
<b>TOA</b>	Top of Atmosphere
<b>UTM</b>	Universal Transverse Mercator
<b>VIS</b>	Visible spectrum
<b>WRS</b>	Worldwide Reference System

# 1

## Introduction

Due to the Arctic amplification, high latitudes are currently undergoing a more intense and faster global warming than other parts of the world, inducing thawing of the permafrost at a global scale [1]. Approximately a quarter of the terrestrial land areas in the northern Hemisphere are underlain by permafrost. Permafrost is defined as frozen ground remaining at or below a temperature of 0°C for at least two years [2]. Depending on the percentage underlain by permafrost it is classified into four classes; continuous (more than 90% of the area), discontinuous (50 % to 90 %), sporadic (10 % to 50 %) and isolated permafrost (less than 10%) [3]. The permafrost ground is divided into the annual freezing and thawing active layer and the perennially frozen ground below this layer. Biological processes, including the formation and decomposition of organic material, are restricted to the active layer [4]. When permafrost thaws, organic carbon stored in the soil can be mobilized and released as the greenhouse gases CO<sub>2</sub> and CH<sub>4</sub>. Furthermore, permafrost degradation changes the landscape in various ways, including locally confined and abrupt processes forming thermokarst terrain but also relatively uniform and gradual isotropic thaw subsidence [5]. Ground subsidence can have a severe impact on infrastructure [6]. Nevertheless, more infrastructure is required by the expanding resource development in northern regions. Over 175 infrastructure projects have been funded in the Northwest Territories, Canada since 2002. 57% of these projects are roads and highways [7].

Irrespective of global warming, infrastructure construction on permafrost is challenging because it changes environmental conditions, enhancing permafrost thaw and ground subsidence. Roads are often built on embankments to protect the underlying permafrost. Snow drifting in the lee of the road and winter road maintenance lead to snow accumulation at the toe of the embankment [8, 9]. Snow has five to twenty times lower thermal conductivity compared to mineral soil [10]. Consequently, snow cover is an effective insulator and prevents the

soil from cooling during the winter months [11]. However, the insulating effects of snow are linked to snow depth, a thin snow cover may result in a cooling of the underlying soil because of the high albedo and emissivity of snow [10] and the insulating effect increases with snow depth [12]. Process-based land surface model results by Park et al. [13] showed that permafrost loss is more significant when snow depths increase in autumn rather than in winter, due to insulation of the soil resulting from early cooling, especially in areas with continuous permafrost.

Snow accumulation and water ponding at the shoulder and toe of the embankment were identified as key processes for increased soil temperatures and road degradation [14]. Roads can interrupt the natural channel drainage and result in water ponding at the embankment toe. Ponding is often related to the upstream side [15–17] due to clogging, bowing or poor inlet conditions of the culverts [16] or because of interception of the suprapermafrost water flow [17]. Grandpre et al. [18] measured ground temperatures under the side slope of a road embankment of the Alaska Highway. The ground temperatures were around 0 °C between September and November which implies high soil moisture, delaying the freeze back of the soil due to latent heat (zero curtain effect). Suprapermafrost water flow over land or in channels during winter, which is inhibited by a road embankment, can lead to upstream pressure within the confined thawed layer leading to an uplift of the overlying frozen materials and formation of injection ice [19]. Continuing water supply can lead to pressure release through fissures allowing the development of surface icings or "aufeis" [20].

Another road-related impact is the dust loading from gravel roads on the surrounding terrain. Road dust on snow has lower albedo, resulting in an earlier spring snow-melt and, consequently, increasing thaw-depth [21]. The dust loads decrease logarithmically and most dust falls within a zone of 300 m while areas beyond are largely unaffected [22]. Auerbach et al. [23] compared the effects of road and road dust disturbance on acidic and non-acidic tundra. They found that despite higher graminoid biomass near the road in both tundra types and higher deciduous shrub biomass in non-acidic tundra, total biomass was lower near the road in both tundra types. Tall shrubs with relatively low nutrient use efficiencies may be favored as the soil nutrient availability increases with the dust deposition [24]. The shrubs may act as a windbreak,



altering the insulating effect of the snow cover because of snow accumulation on and leeward of shrub patches [25]. Furthermore, tall shrubs reduce light, water, and nutrient availability for mosses and heavy dust deposition kills low-growing mosses and lichens [26]. Reduced moss cover and thickness may lead to less thermal insulation of the ground in summer, further amplifying soil warming.

Roads have a linear structure, often intersecting varying terrain with different ecological and hydrological environments over a long distance. In situ measurements help to derive important information on processes on a local scale. However, such local information may not be applicable or extendable to another region along the road. Remote sensing has the benefit of broad spatial and temporal coverage, which can retrieve physical surface parameters serving as indicators of permafrost degradation on a larger scale. Previous studies have used multispectral SPOT imagery (Satellite pour l'Observation de la Terre) to quantify the dust deposition pattern along the Dalton Highway in Alaska [27]. Time series of Unmanned Aerial Vehicle (UAV) baseline datasets were used along sections of Dempster highway and Inuvik to Tuktoyaktuk Highway (ITH) to examine thaw-related creep of road embankments and terrain uplift due to injection ice [19]. Moreover, Landsat image-derived biophysical indices have been utilized to evaluate the impacts of oil and gas development in west Siberia [15]. However, dust deposition on vegetation leaves has been shown to alter the spectral response of the leaf and thus, negatively biasing the Normalized Difference Vegetation Index (NDVI), which is used as an estimate of vegetation biomass [28].

In the scope of the expansion of infrastructure construction in northern regions and its influence on permafrost, this work aims to examine drivers of permafrost degradation using remote sensing techniques. The focus of the study is the regions adjacent to a gravel highway built on permafrost. Few studies have focused on the relatively new (opened in 2017) ITH, which is the first Canadian highway entirely constructed on thaw sensitive continuous permafrost [29]. During the construction, many measures were taken to protect the underlain permafrost. For example, the construction took place during the winter months, the organic cover was left in place, culverts were installed at all low points to enable surface water movement and the road is watered to reduce the dust effects [29]. Despite these measures, the road will likely impact

the permafrost below and in its vicinity. Therefore, more research is required to detect and monitor the changes along ITH and in the adjacent regions.

In this work, five physical parameters are identified as potential permafrost degradation drivers which additionally can be examined with means of remote sensing: (I) snow accumulation [12–14], (II) vegetation moisture [15], (III) water ponding [14–17], (IV) snowmelt [21] and (V) vegetation [21, 24, 28]. Against this background, the hypotheses that guide this work are:

1. Snow accumulates next to the embankment toe.
2. Vegetation moisture content and surface water increase in poorly drained areas along the embankment toe.
3. The snow melts faster in the vicinity of the highway.
4. Vegetation increases along the road.

# 2

## Datasets & Methods

In the following, the study area and the different characteristics of the datasets are explained. Subsequently, the pre-processing steps and methods for investigating the specified research questions are described. I predominantly pre-processed the Sentinel-2 and Landsat-8 using the Google Earth Engine (GEE) python application programming interface (API). GEE provides cloud computing service over a web-based interactive development environment (IDE) or over python API for big data analysis and visualization of geospatial data.

### 2.1 Study Area

The study site is the ITH, which is a 137 km all-weather gravel highway to the east of the Mackenzie Delta in Northwest Territories, Canada (Fig. 2.1). It is located within the continuous permafrost zone in the Beaufort Mackenzie Basin. It traverses the physiographic regions Anderson Plain and Tuktoyaktuk Coastlands [30]. The region south of the treeline (white dashed line in Fig. 2.1) is characterized by a mix of tundra (lichen, mosses, herbs and low shrubs) with heights below 0.5 m, shrub tundra (deciduous shrubs) with heights between 0.5 m to 3.0 m, tall shrub (1.25 m to 3.0 m) and trees (black spruce) above 3.0 m [31]. Sedges, grass, ericaceous shrubs and lichens dominate the low arctic tundra at the northern side of the treeline [32].

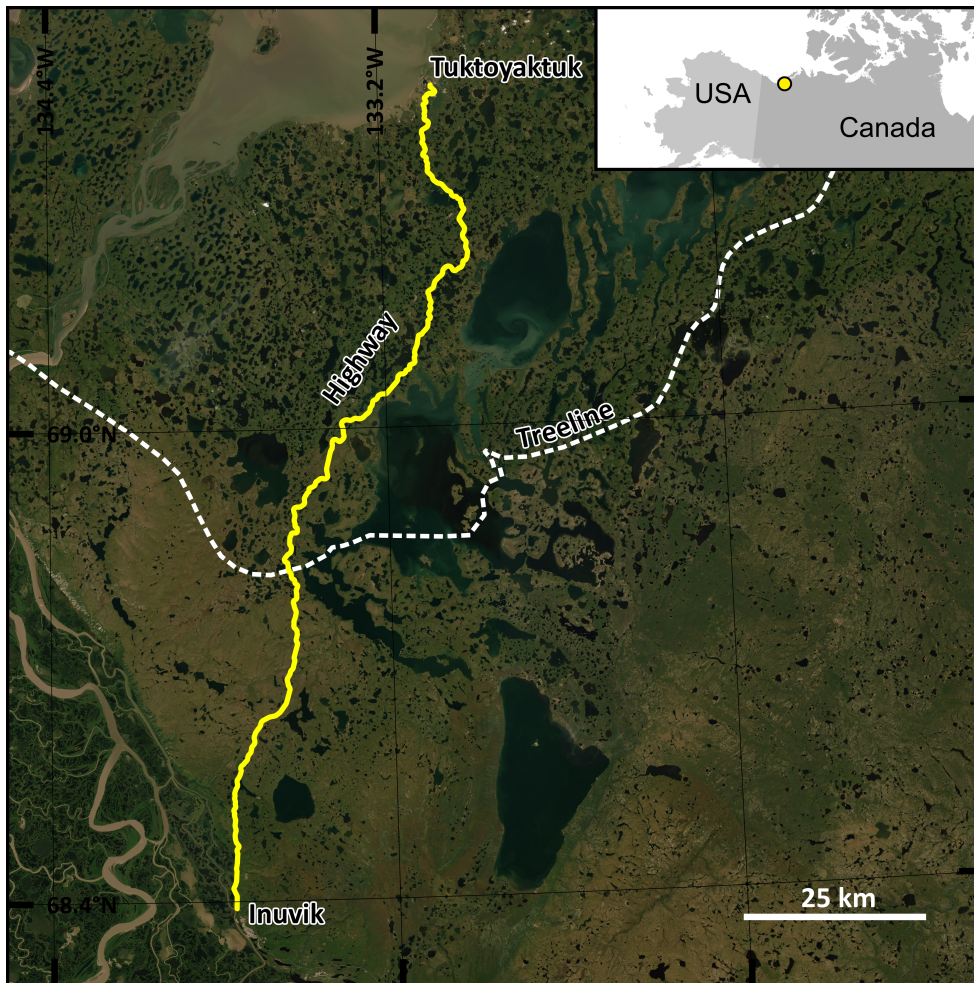


**Figure 2.1:** The study area in Northeast Territories, Canada. The map shows the ITH in Universal Transverse Mercator (UTM) Zone 8 projection. The tree-line is from [33] and the underlying base map source is ESRI satellite (Sources: Esri, DigitalGlobe, GeoEye, i-cubed, USDA FSA, USGS, AEX, Getmapping, Aerogrid, IGN, IGP, swisstopo, and the GIS User Community). The inset map indicates the location of the study area (yellow dot) in Canada.

The elevation above sea level along the route is illustrated in Fig. 2.2. The first half of the route, beginning at Inuvik, is generally located at higher elevations above sea level than the second half. The maximum elevation of 140 m is at 35 km from Inuvik and close to Tuktoyaktuk the minimum elevation of  $-5$  m at 137 km is found. The landscape is characterized by a lake-rich, hummocky and rolling terrain with predominantly ground moraine (fine-grained and stony tills) subsurface materials originating from the Glacial Episode in Late Wisconsin [34] with some interceptions of Alluvial, Glaciofluvial and Lacustrine

deposits. These subsurface materials are frequently ice-rich and consequently sensitive to climate change [35].

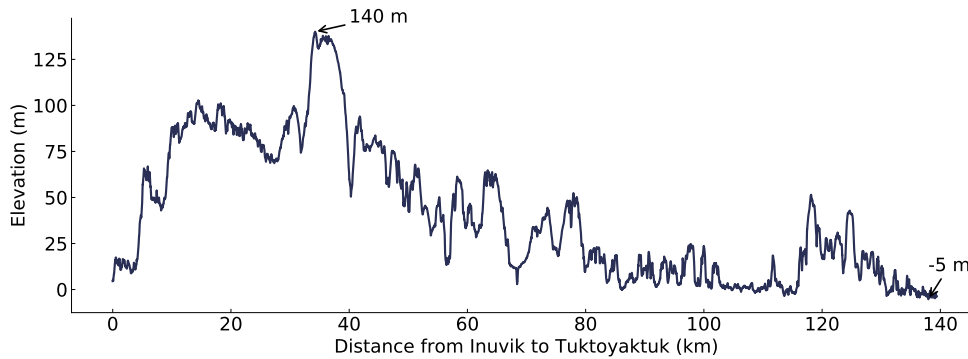


**Figure 2.2:** Profile elevation of ITH from Inuvik (beginning at the distance 0 km) to Tuktoyaktuk. The maximum and minimum elevations are annotated with arrows. The elevations are derived using the Arctic Digital Elevation Model (DEM) [36]. For the filling of closed depressions and re-sampling of the ArcticDEM to 10 m I used QGIS.

The mean annual air temperatures 1990–2020 were  $-7.1$  and  $-8.9$  °C at Inuvik and Tuktoyaktuk, respectively [37]. The monthly mean air temperatures in Inuvik for the years 2016–2020, which represent the years of main focus in the work, are shown in Fig. 2.3. In Tuktoyaktuk the temperature graphs look similar to Inuviks and hence, it is not included in the illustration. The month with the highest temperatures was in July 2017, with a mean temperature of  $15.5$  °C. The year 2020, meanwhile, shows the lowest air temperatures for July with a mean temperature of  $11$  °C. Furthermore, January 2020 was the coldest month in the time series, with the mean air temperature reaching  $-27.7$  °C. The mean annual ground temperatures range from approximately  $-1$  °C in the taiga regions near Inuvik to approximately  $-6$  °C in low-shrub tundra near Tuktoyaktuk [38]. The permafrost depth ranges from 100 m near Inuvik to 500 m in the northern parts of the study area [38].

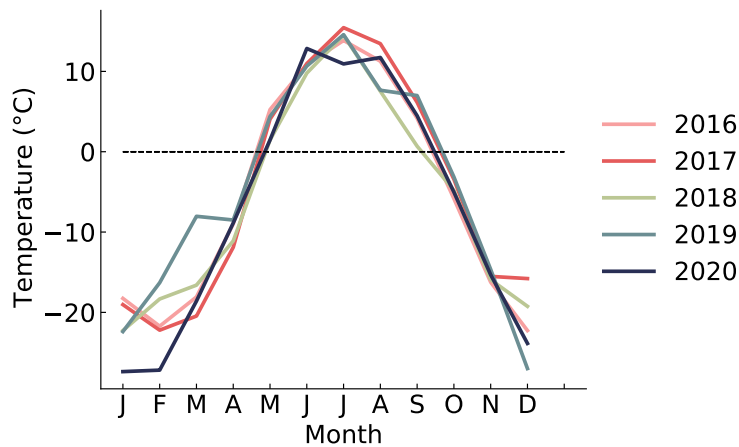


**Figure 2.3:** Monthly mean air temperature in Inuvik (2016–2020) [37].

The highway’s construction began in 2014 and officially opened in 2017. The highway (8 m to 9 m wide) is built on an embankment (with 33% side slopes) to protect the underlying thaw-sensitive permafrost [39]. The embankment height varies along the road depending on the underlain terrain and ice content. The embankment height is 1.4 m for terrain characterized as relatively dry, ice-poor and stable (till and outwash deposits). For till and outwash deposit terrain with medium to rich ice content, the embankment height varies from 1.4 m to 1.6 m. The embankment height for regions with ice-rich permafrost (wet silts and clays or thick organic peatlands) ranges from 1.6 m to 1.8 m [39].

## 2.2 Airborne Laser Scanner Data

The method to analyze the snow depths along the highway relies on two datasets, one snow-covered and one snow-free DEM. I assumed that only the snow influences the elevation differences. As snow-free dataset, I used an Airborne Laser Scanner (ALS) Digital Terrain Model (DTM) (not yet published) with a spatial resolution of 1 m in the coordinate system WGS 1984, UTM 8N (EPSG 32608) from the 22 August 2018. Alfred Wegener Institute (AWI) conducted the second ALS dataset during an ALS survey onboard the AWI's POLAR-5 science aircraft on 10 April 2019, as the landscape was snow-covered. The laser scanner was a Riegl VQ-580 which is specially designed to measure on snow and ice [40]. According to Climate Change Initiative (CCI) standards, the dataset format was binary point cloud data of processing level 1b, which means the data has been converted to sensor units, according to Climate Change Initiative (CCI) standards.

To create a DEM from the binary point-cloud data, I extracted the xyz-data and applied an atmospheric backscatter filter using the python-package awi-als-toolbox [41]. Then, I indexed and chunked the point clouds into tiles with a temporary buffer of 20 m to avoid edge artifacts during the classification using LAStools. To classify the ground points from non-ground points, I applied the Simple Morphological Filter (SMRF), which is based on the approach outlined in [42]. I interpolated the ground-classified dataset with inverse distance weighting (IDW) using the Points2Grid approach integrated into the Point Data Abstraction Library (PDAL). Points2Grid uses a circular neighbourhood defined around each grid cell a search radius = grid resolution \*  $\sqrt{2} / 2$ . I saved the final gridded dataset as GeoTIFF with 1 m cell size and the coordinate system NAD83 / UTM zone 8N (EPSG: 26908).

This work will focus on the intersection of the datasets and the sections that cover ITH. I reprojected the snow-covered dataset to EPSG 32608, then subtracted the snow-free DEM from the snow-covered DEM to obtain the snow depths and snow distribution. Furthermore, I draw an exact road centerline for the intersecting segments using the ALS datasets as baseline data. Then, I created 500 m long transects ( $n = 3169$ ) perpendicular to the road every 1 m over the ITH centerline using GRASS GIS. I extracted the pixel values from the whole transects but chose to analyze only 150 m centered on the road

since the snow distribution did not show any substantial changes beyond that distance. To test for the accuracy of the snow depths, I used the transects over the road, assuming that the road should be snow-free in both datasets, and therefore, showing no to little difference in elevation. Finally, I created boxplots for the snow accumulation distribution along the transects and classified the transects based on their direction (east-west or north-south). For the boxplots I use the following convention throughout the work: the line in the box is the median and the box top and bottom represent 75 and 25 percentiles (i.e., Q3 and Q1), respectively. The top and bottom whiskers in the boxplot mark values within 1.5 interquartile range (IQR) and outliers are excluded.

## 2.3 Sentinel-2

The Sentinel-2 mission consists of a constellation of two polar-orbiting satellites; Sentinel-2A (launched on 23 June 2015) and Sentinel-2B (launched on 7 March 2017). The satellites provide a temporal resolution of five days at the equator [43]. Due to the overlap between adjacent orbits, the revisit time for the study region is one to three days [43]. One scene has 290 km field of view and the spatial resolution of the 13 bands ranges from 10 m to 60 m spanning the visible (VIS), NIR and SWIR spectrum [44] (see Table 2.1). The images are subdivided into 100x100 km<sup>2</sup> tiles, following the naming convention of the Military Grid Reference System (MGRS) with a UTM/WGS84 projection [43].



**Table 2.1:** The spectral region, wavelength range and spatial resolution of each Sentinel-2 Multispectral Instrument (MSI) satellite band.

Sentinel-2 MSI			
Band	Spectral region	Wavelength range ( $\mu\text{m}$ )	Resolution (m)
B1	Aerosols	0.42 - 0.46	60
B2	Blue	0.44 - 0.53	10
B3	Green	0.54 - 0.58	10
B4	Red	0.65 - 0.68	10
B5	Red Edge 1	0.69 - 0.71	20
B6	Red Edge 2	0.73 - 0.75	20
B7	Red Edge 3	0.77 - 0.80	20
B8	NIR	0.77 - 0.91	10
B8A	Red Edge 4	0.85 - 0.88	20
B9	Water vapor	0.93 - 0.96	60
B10	Cirrus	1.34 - 1.41	60
B11	SWIR 1	1.54 - 1.68	20
B12	SWIR 2	2.07 - 2.31	20

Bottom of Atmosphere (BOA) reflectance (Level-2A product) Sentinel-2 products are provided by GEE from 2017 onward. For consistency of the images, I chose to work with the orthorectified and map-projected top of Atmosphere (TOA) Reflectance Level-1C Sentinel-2 products with availability from 2015 onward. However, only images from 2016 and onward were available for the study site. The workflow included the pre-processing steps (I) initial filtering, (II) atmospheric correction, (III) cloud and cloud shadow masking followed by (IV) indices calculation, (V) co-registration and (VI) pixel-based analysis (Fig. 2.4).

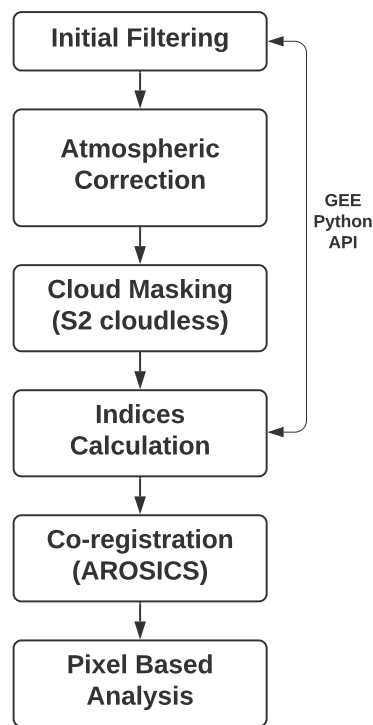


**Figure 2.4:** Processing steps for the Sentinel-2 data.

### 2.3.1 Initial Filtering

The processing chain of the Sentinel-2 imagery started with image selection and filtering of the image collection, using only images for the period July and August. These months represent the peak growing season and have also been used in e.g. [15] to analyze land cover changes along with anthropogenic disturbances in the Arctic. In an initial step, I selected all images for 2016–2020 with cloud cover less than 20 %. I also chose the MGRS tile 08WNB from orbits 14, 57, and 100 as the initial filter because it included the whole research area. I noticed that the image collection on some dates featured remarkably similar images (same values, same bounding box). The only variation between these images was the time stamp, which differed by a few seconds. Therefore, I visually inspected the images to delete duplicates. Furthermore, I removed some images from 2016 because they only represented a small segment of the study area. Further, I manually removed one image from 12 July 2017 from the image collection since the image showed very high brightness compared to the other images. The initial filtering resulted in a total of 28 images for

all years, 2 images for 2016, 7 for 2017, 5 for 2018, 7 for 2019 and 7 for 2020 (Figure 2.5)

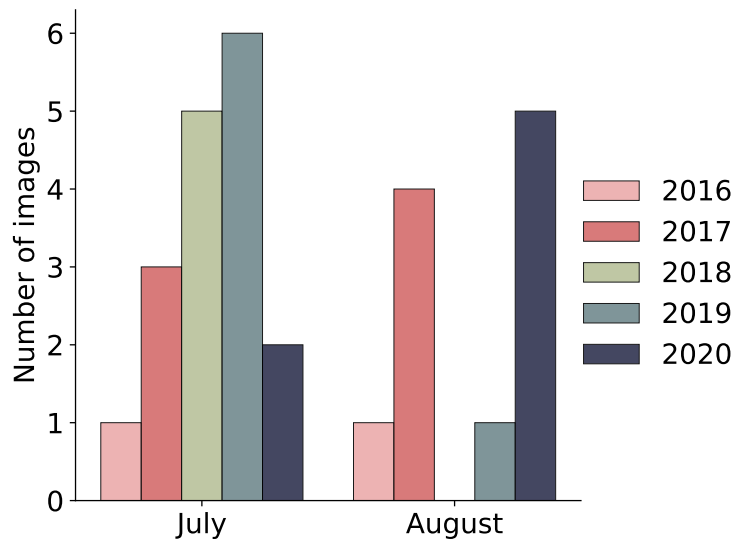


**Figure 2.5:** Number of utilized Sentinel-2 images per year and month.

### 2.3.2 Atmospheric Correction

The electromagnetic radiation reflected from the ground and recorded by a sensor is influenced by atmospheric interactions, such as scattering and absorption of radiation by clouds, aerosols and gases [45]. The quality of vegetation indices and spectral signals, extracted by satellite measurements, is negatively influenced by atmospheric effects [46]. Therefore, I applied an atmospheric correction to obtain Level-2A BOA products from the Level-1C TOA using the open-source tool 6S (Second Simulation of the Satellite Signal in the Solar Spectrum) [47] with GEE in an interface through Python (Py6S) [48] with a code based on [49]. The Py6S has been tested and evaluated for the quality of the Level-2 A in [50]. First, I converted the TOA reflectance  $R_{TOA}$  to TOA radiance ( $L_{TOA}$ ) with the formula:

$$L_{TOA}(\lambda) = \frac{ESUN(\lambda) \cos(\theta) R_{TOA}(\lambda)}{\pi d^2} \quad (2.1)$$

where  $ESUN(\lambda)$  is the solar exoatmospheric spectral irradiance in wavelengths

corrected for daily variations,  $\theta$  solar zenith angle in radians and  $d$  the Earth-Sun distance [49].

The TOA radiance can further be described as follows:

$$L_{TOA} = \tau\rho(E_{dir} + E_{dif})/\pi + L_p \quad (2.2)$$

where  $L_{TOA}$  is TOA radiance,  $\tau$  is transmissivity,  $\rho$  is surface reflectance,  $E_{dir}$  is the direct solar irradiance,  $E_{dif}$  is diffuse solar irradiance and  $L_p$  is path radiance. The four unknown atmospheric terms ( $\tau$ ,  $E_{dir}$ ,  $E_{dif}$  and  $L_p$ ) are solved using the 6S radiative transfer code considering atmospheric parameters like the total amount of water and ozone in a vertical path through the atmosphere and the aerosol optical thickness value. These atmospheric parameters are derived from the image metadata. The parameter altitude of the target is specified using the ArcticDEM [36]. Therefore, the surface reflectance can be solved as follows [49]:

$$\rho = \pi(L_{TOA} - L_p)/\tau(E_{dir} + E_{dif}) \quad (2.3)$$

Figure 2.6 gives an example of a true color composite before (Fig. 2.6a) and after atmospheric correction (Fig. 2.6b) with Py6S depicting the visual improvement after the correction.

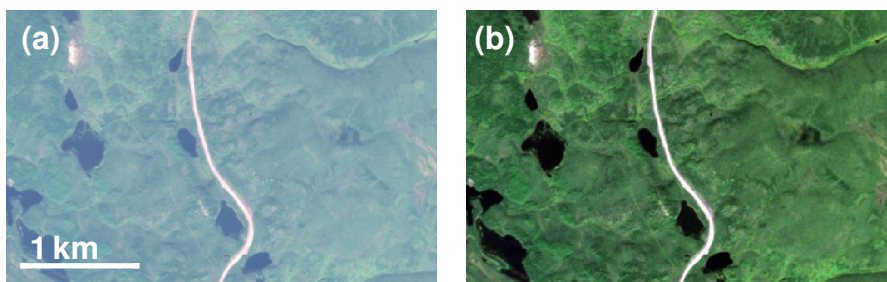


**Figure 2.6:** True color composites of (a) TOA reflectance of a Sentinel-2 image of 19 August 2017 and (b) BOA reflectance of the same image after atmospheric correction with Py6S.

### 2.3.3 Cloud Masking

The detection and masking of clouds and cloud shadows are mandatory when working with optical remote sensing since the measured electromagnetic signal is affected by cloud presence which thus alters the received information [51]. Cloud and cloud shadow masking is essential in northern regions where persistent cloud cover has been identified as one of the major limiting factors (besides steep sun angles and low light intensities) for passive satellite systems [52].

In this work, I used the machine learning-based cloud detector S2cloudless, which has been developed by Sentinel Hub’s research team using as ground truth the cloud masks produced by MAJA [53]. Compared to other widely used cloud detection algorithms, S2cloudless has a high cloud detection rate and a lower misclassification rate of land and snow as clouds [54]. Each pixel is assigned a cloud probability based on the pixel’s 10 Sentinel-2 band values [55] and the cloud shadow is defined by cloud projection intersection with low-reflectance NIR pixels [56].

Cloud probability at 10 m scale is provided for every image in the Sentinel-2 archives in GEE, giving each image a corresponding S2cloudless image. The cloud masking has been implemented in the script [56] giving the user the control to decide on different threshold parameters to optimize the masking. In this work, I tested several different thresholds for cloud probability, NIR reflectance and maximum distance to search for cloud shadows from cloud edges on a sample of images. I achieved the best result with 50%, 0.15 and 2 km, respectively. Furthermore, I set a buffer of 50 m to dilate the edge of cloud-identified objects. Fig. 2.7 shows an example of the cloud and cloud shadow detection for a Sentinel-2 image with the customized thresholds. Fig. 2.7a shows a true color composite of a partly cloud-covered landscape with some lakes visible and Fig. 2.7b shows the true color composite with the cloud and cloud shadow masks.

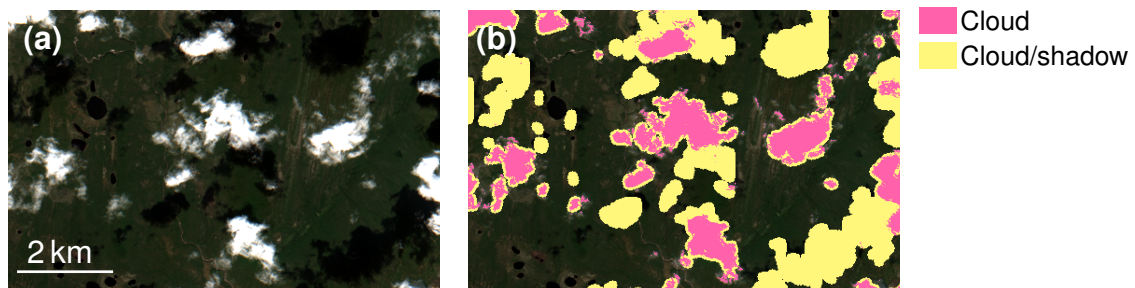


**Figure 2.7:** True color composites of a Sentinel-2 image with (a) visible clouds and (b) the same image with the cloud mask in pink and the cloud and cloud shadow mask including buffer in yellow.

### 2.3.4 Indices

I utilized the Sentinel-2 imagery for the vegetation, water, and moisture analysis. I utilized Sentinel-2 images, knowing the disadvantage of using Sentinel-2 imagery because there were no images before construction. Having images before construction would help to examine how the physical parameters' values and spatial patterns were dispersed in the original and undisturbed landscape. However, the benefit of using Sentinel-2 images is the finer spatial resolution compared to Landsat (Fig. 2.8), making it more likely to identify small scale changes along the road. From the atmospheric corrected, cloud and cloud shadow masked Sentinel-2 imagery, I calculated the indices Normalized Difference Moisture Index (NDMI), Normalized Difference Water Index (NDWI) and NDVI in GEE Python API.

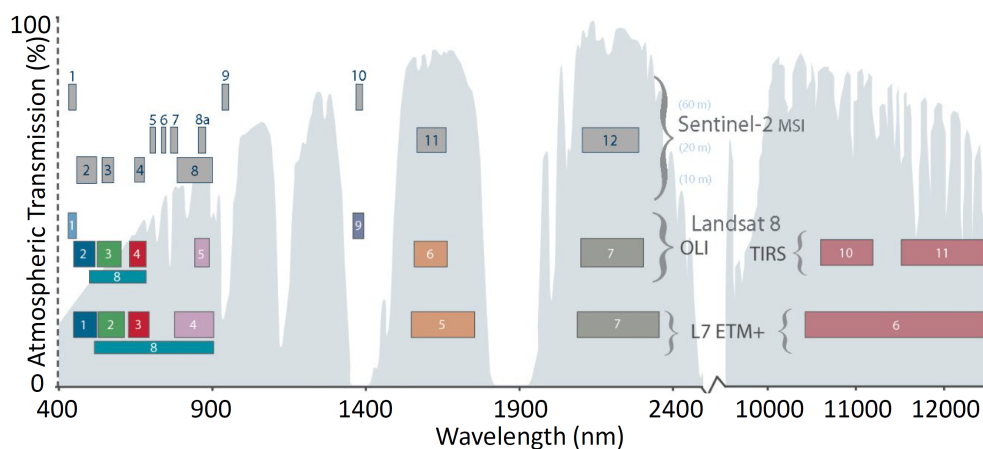


**Figure 2.8:** Bandwidths and band names for Landsat-7, Landsat-8 and Sentinel-2. Modified after [57]

NDMI is sensitive to liquid water in vegetation and is computed using the short-wave-infrared (SWIR) and NIR reflectance [58]. NIR reflectance is affected by the leaf dry matter and the leaf internal structure but not by the water content. At the same time, the SWIR band reflects changes in both the vegetation water content and the mesophyll structure. By combining these two bands, the variation induced by leaf internal structure and leaf dry matter content is removed and thus, improving the accuracy in retrieving the vegetation water content [59]. The values range from -1 to 1, with negative values indicating water stress and positive values indicating water logging [60]. NDMI is defined as follows:

$$NDMI = \frac{(NIR - SWIR)}{(NIR + SWIR)} \quad (2.4)$$

NDWI was proposed by [61] to delineate open water features. The index aims to use the green band to maximize the reflectance of the water body and the high absorption of NIR wavelengths to minimize it [61]. It is defined as the difference between the green and NIR bands divided by their sum. The NDWI values will range from -1 to 1 with water bodies having positive values whereas soil and terrestrial vegetation features having zero or negative values [61] and is defined as follows:

$$NDWI = \frac{(Green - NIR)}{(Green + NIR)} \quad (2.5)$$

When inspecting the output raster images, I revealed a limitation of using the NDWI to extract information about possible water ponding along the road. According to [61], water bodies should have positive values, whereas build-up areas and vegetation should have negative values. This index relies on the typically higher reflectance of NIR and low reflectance of green wavelengths for vegetation (giving negative values) and a higher reflectance of green wavelengths than the NIR for water bodies (giving positive values).

However, some water bodies in the study area show negative values (Fig. 2.9),

which means that for these water bodies, the green reflected light is lower than the NIR. This finding reveals that NDWI is insufficient for analyzing water ponds along the road. The road has negative values, as well as little water ponds with shallow water close to it. This atypical appearance of water pixels in the visible spectrum is typical at high latitudes where low sun zenith and shallow water bodies promote sun glint, turbidity and lake bottom reflectance [62]. Instead, I used only the NIR band to analyze any changes of open water bodies along the road, relying on water's high absorption in NIR compared to non-water areas [63–65].

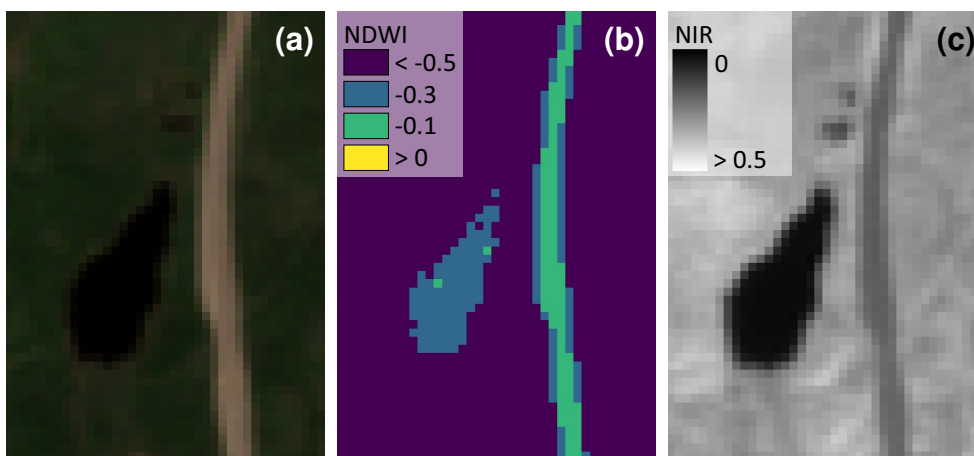


**Figure 2.9:** Water body and small water ponds next to ITH displayed in (a) true colors, (b) NDWI and (c) NIR from a Sentinel-2 image (from 20 Januar 2018) with a resolution of 10 m.

NDVI can be used as an indicator to quantify the greenness of plants because of the inverse relationship between vegetation brightness in the red and near-infrared (NIR) spectrum. Healthy vegetation absorbs red light by the chlorophyll and has a high reflectance in the NIR region due to high scattering in the mesophyll tissue. In contrast, unhealthy vegetation reflects more red radiation and less NIR [66]. Consequently, healthy vegetation will have a higher NDVI. NDVI values lower than 0.1 correspond to bare soil or snow [67]. Moderate NDVI levels may be a result of sparse vegetation like shrubs and grasslands or by senescing crops (approximately 0.2 to 0.5) [67]. The NDVI is calculated as follows:



$$NDVI = \frac{(NIR - Red)}{(NIR + Red)} \quad (2.6)$$

### 2.3.5 Co-registration

Misregistration of images occurs between sensors or even within a sensor. For Sentinel-2 the nominal geolocation uncertainty reach up to 12.5 m [68], which is more than one pixel. The displacements of the images, might negatively influence the results, especially when analyzing changes along a road, where the spatial extent of the hypothesized changes is rather small. Therefore, after downloading the images from GEE, I conducted a subpixel co-registration of the images using a local co-registration tool in the Automated and Robust Open-Source Image Co-Registration Software (AROSICS 2.0) [69] in Python. In the local co-registration, a reference image and a target image are used to detect the geometric shift using a moving window for each point of a dense grid. The detected tie points are subsequently validated using a multistage workflow described in [69]. To compute the parameters of an affine transformation, only those tie points that aren't tagged as false-positives are employed [69]. As a reference image, I used a cloud-free Sentinel-2 image from 28 August and I set the moving window size to  $256 \times 256$  pixels and maximum iterations to 10.

### 2.3.6 Pixel-based Analysis

I used the NDVI band from one image 2016 to vectorize all the road area (including embankment) in QGIS using a threshold of 0.4. Using the vectorized road, I could derive the road's centerline in QGIS. To quantify the distance effect of the road, I generated 120 buffers in 5 m intervals along the vectorized road, excluding the road and embankment (Fig. 2.10a). I chose the maximum distance of 600 m assuming that areas beyond this distance remain undisturbed. Furthermore, I created a 20 m buffer zone around the road, excluding the road and embankment (Fig. 2.10b) and divided the polygon into upstream and downstream sides, based on the watersheds from Ensom, T. (unpublished data), for the water ponding analysis.

I extracted the pixel values in each buffer zone using the extract function

in the eo-box Python package [70]. At the moment, eo-box can only handle single-band images [70]. Therefore, I extracted the bands in the multiband images using the translate utility in the Geospatial Data Abstraction Library (GDAL). After extracting all the single bands, I utilized the extract function in eo-box. The function creates a mask by rasterizing the buffer zones using a template raster. The template raster is the first raster in the list by default. That means, that the mask's pixel centers correspond to the first raster's pixel centers. Each image pixel value could be extracted and further quantified using this mask.

The utilized methods and statistics for the pixel-based analysis differ depending on the index. In an initial step, I combined the extracted pixel values for each index into annual pixel stacks. For the study of the NDVI, I calculated the maximum NDVI of each pixel stack. I did this to overcome the influence of different phenological stages. Furthermore, I excluded values below 0.4 from the analysis to ensure that it only implied vegetation [67]. Compared to the NDVI, I used the median value in the annual pixel stacks for the NDMI study. I utilized the median NDMI to eliminate the influence of extreme NDMI values (caused by, e.g., local precipitation). Further, I masked the larger water bodies in the NDMI using the NDWI of a cloud-free image from 2 July 2018. In summary, this resulted in each pixel coordinate storing two values per year: (I) the maximum NDVI and (II) the median NDMI. Then, I grouped each year in 5 m steps from the road edge with the help of the buffer zones. The grouped NDVI and NDMI index values per year and pixel served the distribution analysis.

The absolute values of the indices can fluctuate significantly across years [15], making it difficult to compare the road effect between them. To focus on the road effect exclusively, I normalized the median NDMI and median NDVI on a distance of 500 m. The selection of distance is based on the findings of [22, 28], who found no significant effect of the road after 300 m and 625 m, respectively. Therefore, I used the 500 m distance as a reference site. I achieved the normalization by subtracting the individual annual index value at 500 m from all values in the corresponding year.

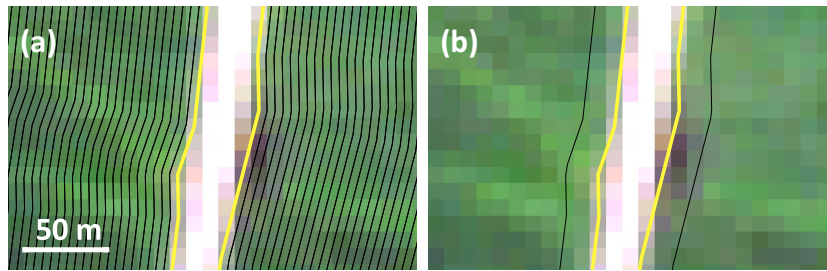


**Figure 2.10:** Sentinel-2 true-color image with (a) the borders of the ITH in yellow and the buffer zones in 5 m steps displayed in black and (b) 20 m buffer zone excluding road and embankment and divided into upstream and downstream.

For the water ponds analysis, I used the NIR bands of the images. Finding a threshold value for water using a not normalized single-band index might be challenging because of different illumination and acquisition geometry of the images [62]. Additionally, the road exhibits low reflectance in NIR and may sometimes show NIR reflectances similar to water (Fig. 2.11).

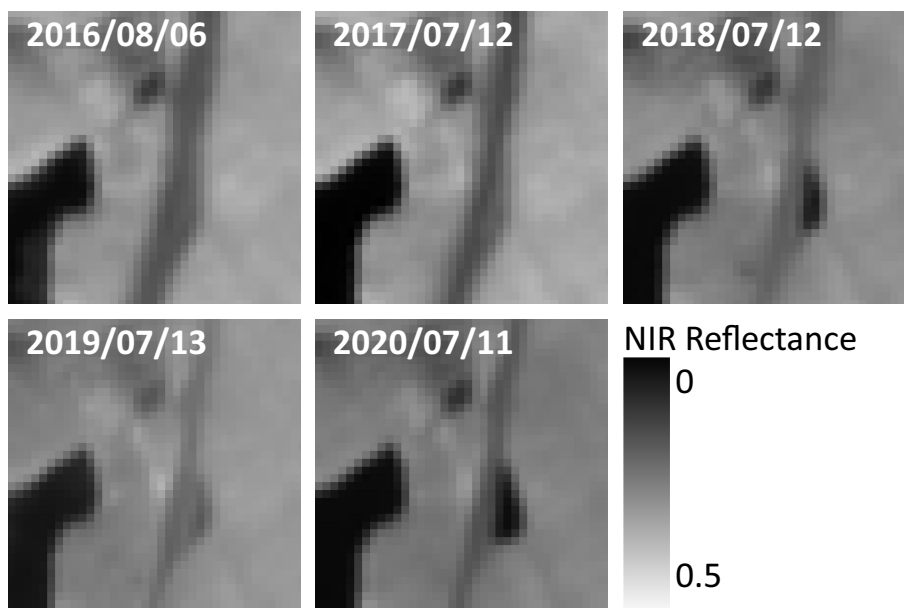


**Figure 2.11:** Development of a water pond in the vicinity of the road through the years visualized with the NIR band from one Sentinel-2 image per year (2016–2020) during the summer months.

I used a threshold value of 0.128 for water, which showed high accuracy in [64]. I visually inspected several images to confirm the threshold's transferability to the scenes used in this work. Then, I calculated the median NIR value for each pixel and year to exclude any outliers from the analysis. Outliers can occur when pixels affected by clouds or cloud shadows are missed during the automatic masking processes [71] (outlined in the section 2.3.3) as well as when local precipitation has influenced the reflectance. Then, in the annual time series, I preserved every pixel that had values equal to or less than the threshold value at least once throughout the pixel time series (Fig. 2.12). I used this method to compare the upstream and downstream sides over the years.

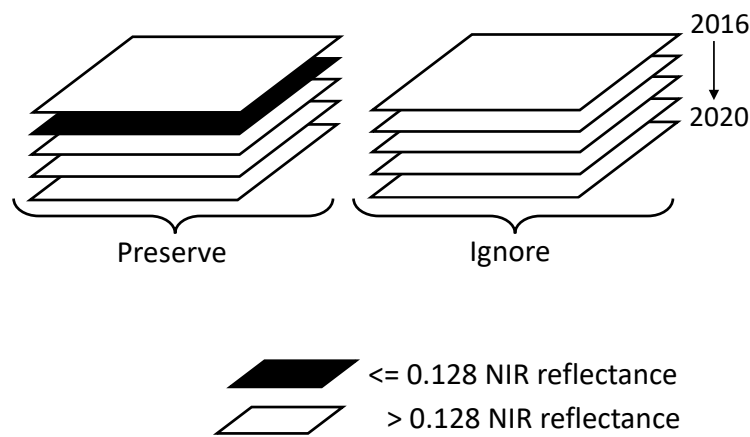


**Figure 2.12:** Illustration of two examples of NIR band pixel time-series. Each square represents a pixel of the median NIR reflectance of the year. I preserved the whole time series if at least one pixel in the time series was below the threshold.

### 2.3.7 Landsat

Datasets before, during and after construction were needed to analyze the snowmelt pattern in the vicinity of the ITH. For this purpose, I utilized Landsat-7 ETM (Enhanced Thematic Mapper) and Landsat-8 OLI (Operational Land Imager) images. The United States Geological Survey (USGS) satellites orbit Sun-synchronously at 705 km altitude with an equatorial revisit time of 16 days [72]. Because of the high side overlap of the WRS-paths (Worldwide Reference System) at the higher latitudes, the study site has a revisit frequency of 3-5 days [73].

Landsat-7 was launched in April 1999 and is still operating. However, a failure of the Scan Line Corrector (SLC) in 2003 results in stripes of missing data on either side of the images [72]. Landsat-8 was launched in February 2013. The spatial resolution for the Landsat-8 bands ranges from 15 m (panchromatic), 30 m (VIS, NIR, SWIR) to 100 m (thermal) (Tab. 2.2).

**Table 2.2:** The spectral region, wavelength range and spatial resolution for each Landsat-8 OLI satellite band.

Landsat-8 OLI			
Band	Spectral region	Wavelength range ( $\mu\text{m}$ )	Resolution (m)
B1	Coastal aerosol	0.43 - 0.45	30
B2	Blue	0.45 - 0.51	30
B3	Green	0.53 - 0.59	30
B4	Red	0.64 - 0.67	30
B5	NIR	0.85 - 0.88	30
B6	SWIR 1	1.57 - 1.65	30
B7	SWIR 2	2.11 - 2.29	30
B8	Panchromatic	0.52 - 0.90	15
B9	Cirrus	1.36 - 1.38	15
B10	Thermal infrared 1	10.60 - 11.19	30*
B11	Thermal infrared 2	11.50 - 12.51	30*
BQA	QA Bitmask		

\* resampled from 100m to 30m

The band names and bandwidths differ slightly between Landsat-7 and Landsat-8. Furthermore, Landsat-8 has two new spectral bands not present in Landsat-7; a coastal/aerosol band (band 1) and a cirrus band (band 9) (Fig. 2.8). Atmospherically corrected surface reflectance images are available from the two satellites on GEE for all years. Therefore, no pre-processing of the images is needed. The snowmelt pattern analysis followed the workflow in Fig. 2.13. I selected one cloud-free image per year in May-June, which corresponds to a period when the snow is partially melted in the landscape. To illustrate "before construction conditions," I utilized one image from 2002 (Landsat-7) and one image from 2013 (Landsat-8) and Landsat-8 for the period during and after road construction. I calculated the Normalized Difference Snow In-

index (NDSI) for all images. NDSI helps to discriminate snow, ice and water from bare soils and clouds [74] by taking advantage of the high exoatmospheric reflectance characteristics of snow and ice in the visible spectrum and the absorption in SWIR1. It is defined as the difference between the green band and the SWIR1 band divided by their sum [75]:

$$NDSI = \frac{(Green - SWIR1)}{(Green + SWIR1)} \quad (2.7)$$

According to [75], ice, snow, and water were identified by a surface reflectance threshold value of  $> 0.4$ , whereas bedrock and bare soils were identified by a value of  $< 0.4$ . Therefore, I used this threshold in this work. I created a water mask using the NDWI of a snow-free image from August 2019 and applied it to all images to remove the water bodies.

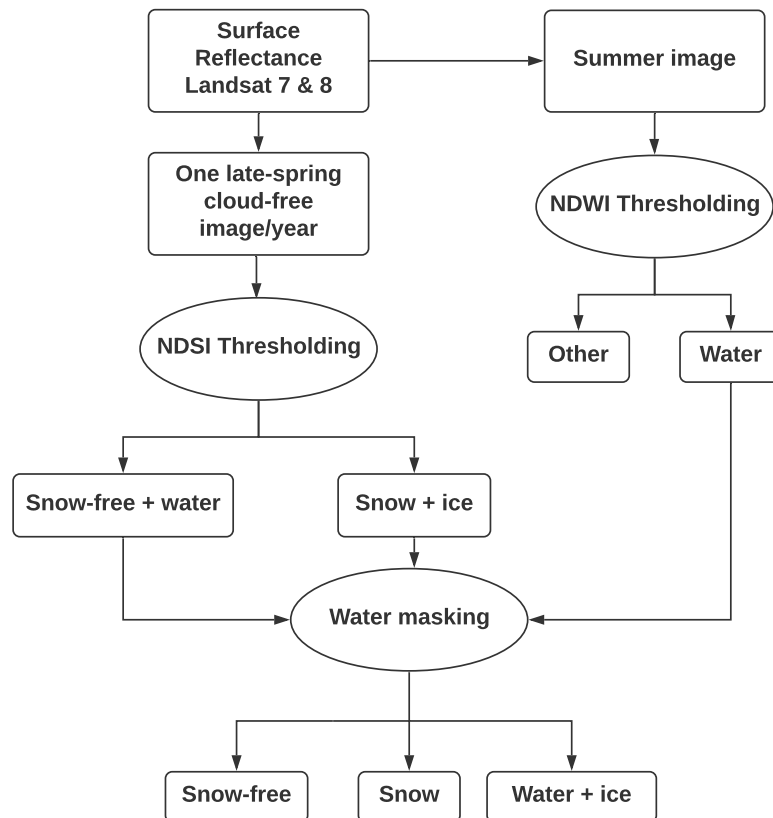


**Figure 2.13:** Process chain for snow discrimination using Landsat data.

The product was one raster image for each year with pixels with values of 0 indicating ice-covered water bodies or open water, values of 1 indicating snow and values of 2 indicating snow-free areas (Fig. 2.14). For the pixel-based analysis, I used the 5 m buffer zones along the road created in section 2.3.6 as well as the same workflow to extract the pixel values.

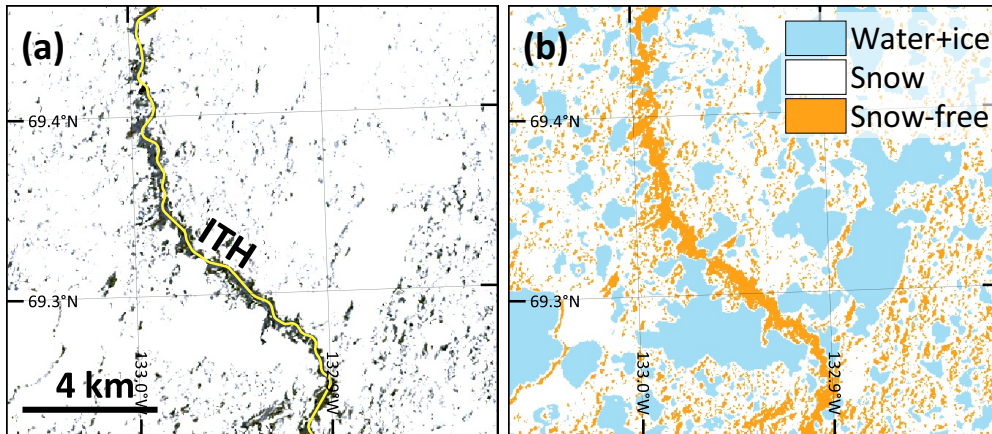


**Figure 2.14:** (a) A true color composite from a Landsat-8 image with snow cover from a partly melted landscape (5 May 2018) and (b) threshold NDSI values with snow-covered pixels shown in white and snow-free pixels shown in orange, the water bodies in blue were masked using the NDWI from an image in late summer.

# 3

## Results

### 3.1 Snow Accumulation

The main result of the ALS point cloud processing is a DEM over a snow-covered landscape. I obtained the snow depths as visualized in (Fig. 3.1) by subtracting a snow-free DEM from the snow-covered DEM. The total length of the road covered by both the snow-free and snow-covered DEM is 4.4 km. The spatial distribution of the snow depths appears to be in accordance with the underlying terrain of the area. There is less variation and smaller snow depths on the flat tundra terrain and greater snow depths at valley slopes and along the embankment toe of the road. The only snow-free feature distinguishable in the map is on top of the road, indicating active snow removal before the ALS data was collected. By visually inspecting the map, it seems that more snow has accumulated on the western side of the road. The average snow depth of the surrounding tundra reaches about 40 cm (Fig. 3.1).

I extracted the pixel values from the snow-free and snow-covered DEM from 150 m long transects with 1 m spacing to validate the snow-covered DEM and to quantify and visualize the snow accumulation along the road (Fig. 3.2).



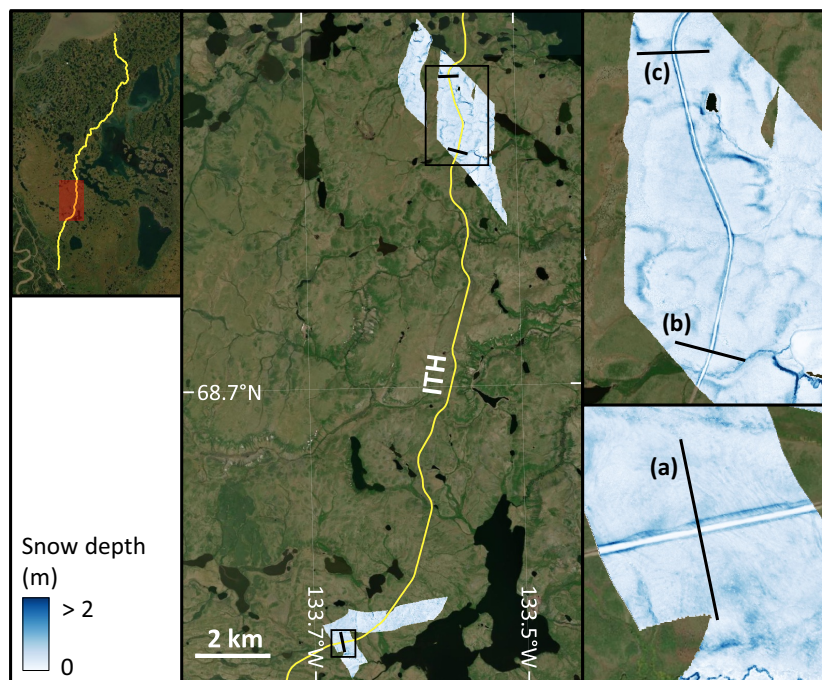
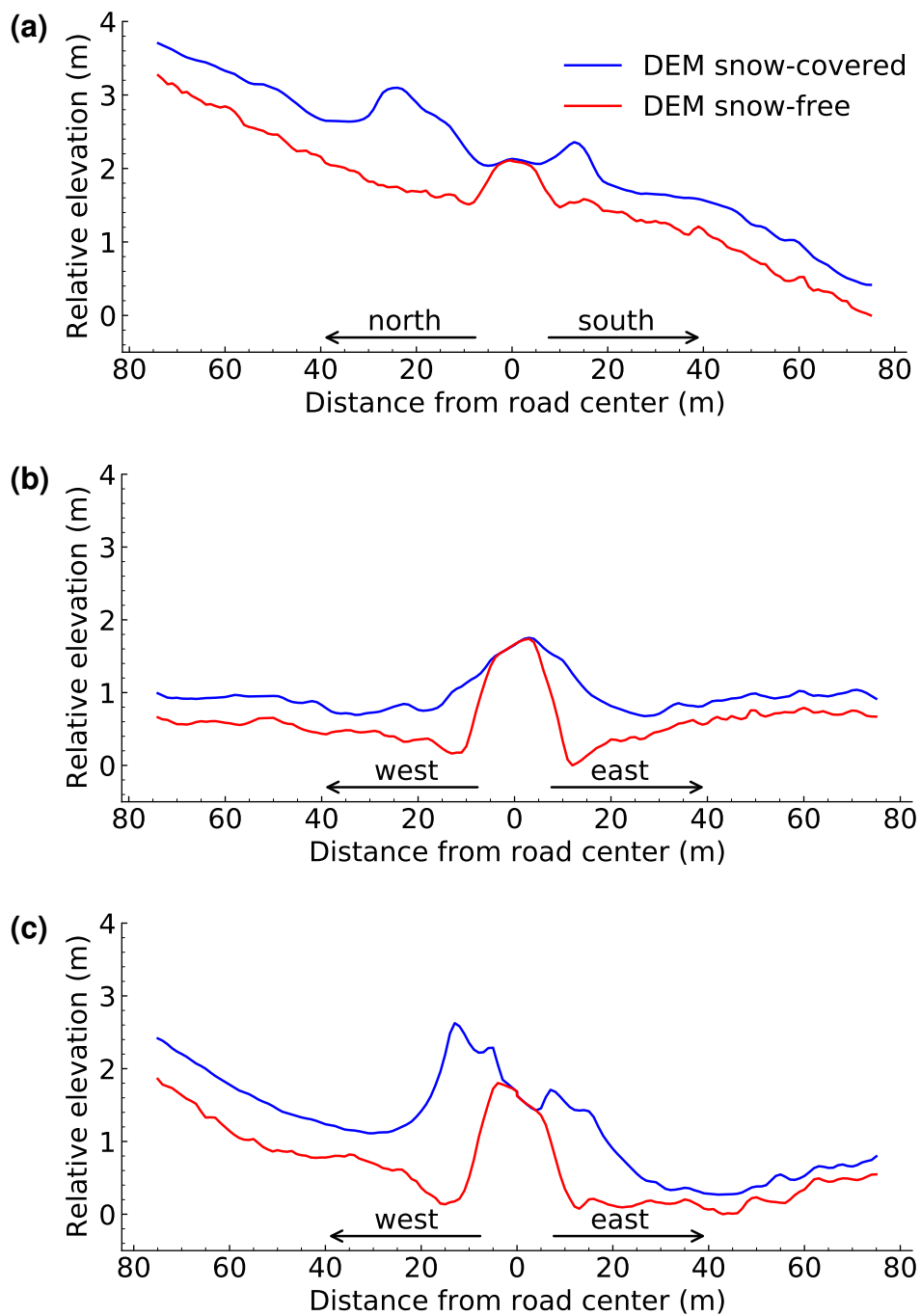


**Figure 3.1:** Snow depths derived from the intersecting regions from one snow-free and one snow-covered DEM along the ITH (yellow line). Example of snow depth transects are marked by blacked lines (not to scale). In total, I extracted and analysed the pixel values of 3169 transects with 1 m spacing.

The transect in Fig. 3.2a is extracted from the southern part of the study area (Fig. 3.1a). Over the 150 m, the elevation decreases 3 m from the north to the south. The embankment height for this transect is 0.6 m. The accumulated snow reaches the maximum depth of 1.4 m at a distance of 23 m from the road center at the northern side of the road. The maximum snow depth of 0.8 m on the southern side is located closer to the road (13 m). Increased snow depth reaches up to 40 m from the road center (northern side) and 17.5 m on the southern side.

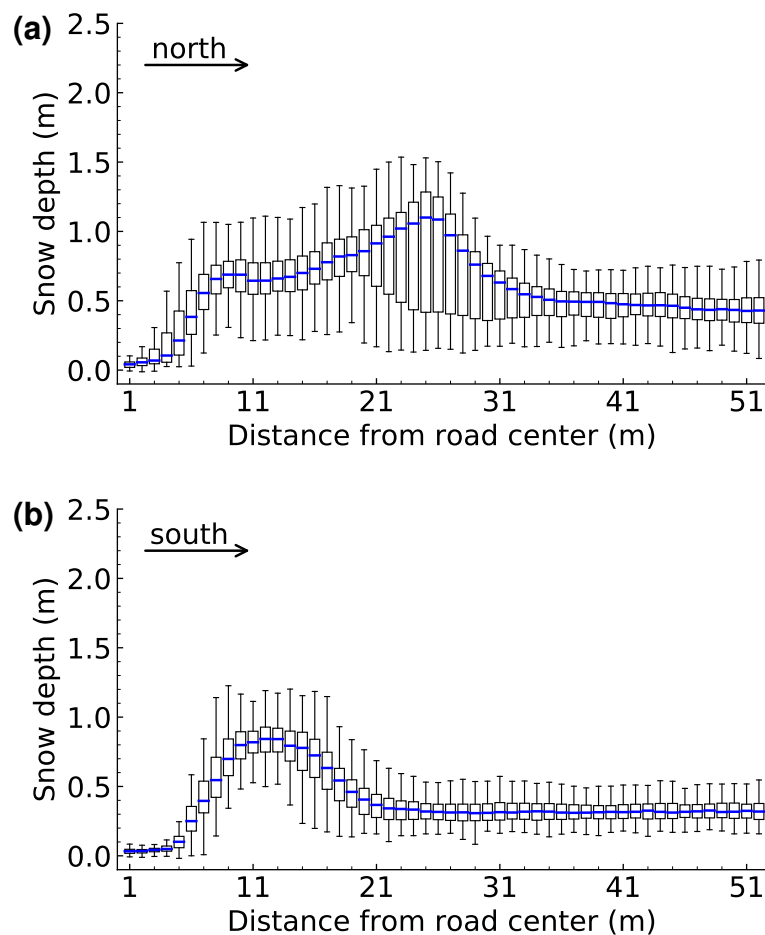
The second transect (Fig. 3.2b) is extracted from the southern part of the study segment located in the north (Fig. 3.1b). The embankment height for this transect is 1.7 m and it is located on a surface with almost flat terrain. The maximum snow accumulation is located in the absolute vicinity of the embankment with snow depths of 0.9 m (western side) and 1.3 m on the eastern side. The snow accumulation enhancement reaches approximately 20 m from the road center on both sides.

Fig. 3.2c depicts the transect with the greatest snow depths out of all 3169, located in the northern part of the study area (Fig. 3.1c). The transect shows two peaks of maximum snow depths on each side of the road. The embankment height is 1.7 m at this transect location with a decrease in relative elevation on both sides towards the road. The snow depth exceeds more than 2.4 m on the western side and 1.3 m on the eastern side. The snow accumulation reaches up to a distance of 20 m on the western and 30 m on the eastern side for this transect. Significant for the transect (Fig. 3.1c) is the generally larger snow depths on the western side on distances beyond 20 m (average of 0.5 m) compared to the eastern side (average of 0.25 m).



**Figure 3.2:** Three example of transects perpendicular to the road with the length 150 m. The figure show the relative elevation in meters of the snow-free DEM (from 22 August 2018) and the snow-covered DEM (from 10 April 2019) from the (a) southern, (b) central and (c) northern part of the study region. The locations of the transects (a-c) are shown in Fig. 3.1

The distribution of the snow depths for all transects in north-south direction ( $n = 400$ ) is visualized in Fig. 3.3. The snow accumulation enhancement reaches up to 36 m from the road center at the northern side with the strongest accumulation between 9 and 26 m from the road center (Fig. 3.3a). The maximum snow depths are located 26 m from the road center with median snow depths of 1 m on the northern side. In south direction (Fig. 3.3b), the snow accumulation enhancement reaches up to 26 m and 12 m from the road center on the southern side the median snow depths are 0.8 m (Fig. 3.3b). The northern side of the road has more variance in snow depths than the southern side. Furthermore, the snow depths further away from the road are generally greater on the northern side (0.5 m) than on the southern side (0.35 m).



**Figure 3.3:** Snow accumulation derived from transects ( $n = 400$ ) on the (a) northern side and (b) southern side of the road. The blue lines are the median depths from the transects.

Compared to north-south direction, more transects in the study area are located in east-west direction ( $n = 400$  versus  $n = 2769$ ). The snow depths distribution for east-west direction are depicted in Fig. 3.4. For the eastern side the snow accumulation reaches up to 26 m from the road center (Fig. 3.4a). Meanwhile, the snow accumulation enhancement reaches up to 36 m from the road center at the western side (Fig. 3.4a). The maximum snow depths are located 10 m from the road center on the eastern side with median snow depths of 0.9 m (Fig. 3.4a). For the western side the median snow depths maximum is at 15 m from the road center with snow depths of 1 m (Fig. 3.4b). As shown by the whiskers in the boxplots, the variation of snow depths increases with increased snow accumulation enhancement for both sides. The variation of snow depths is generally larger on the northern side than the southern side.

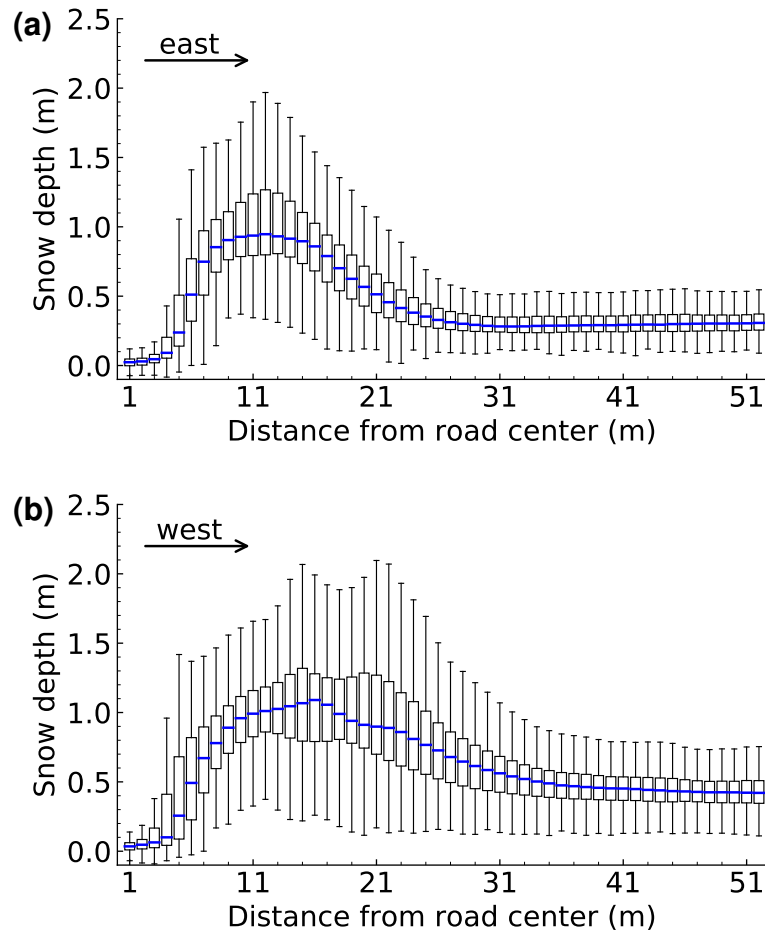


**Figure 3.4:** Snow accumulation derived from transects ( $n = 2769$ ) on the (a) eastern side and (b) western side of the road. The blue lines are the median depths from the transects.

---

## 3.2 Vegetation Moisture Content and Surface Water

I examined the vegetation moisture content changes along the road with means of the median NDMI in the pixel stack in the growing season using Sentinel-2 images for the years 2016–2020. The distribution of all absolute NDMI values for each year and distances up to 60 m is shown in Fig. 3.5a. Note that the distances for this analysis are measured from the road edge (see Fig. 2.10a). Overall, substantial changes in NDMI occurred within the first 15 m from the road for all years with lower NDMI values towards the road, indicating less vegetation moisture there. However, the boxplot pattern shows an effect up to a distance of 25 m, and further away, the pattern of median values remains stable. At the closest distance from the road (5 m), the year 2016 shows the lowest median NDMI. There is a gradual NDMI increase the following years until 2019 and, subsequently, a decrease in 2020, reaching a median value similar to 2017. At 10 m distance from the road edge, there is a transition towards more similar median values for all years. Subsequently, at distances greater than 25 m, there is a reversed pattern between the median values of the years compared to at 5 m. At distances far away, 2016 and 2017 show the highest NDMI and 2018–2020 the lowest. 2016 shows the most significant differences in the first 25 m with the median value increasing from 0.018 to 0.164. Over time, the effect of distance to road has decreased. The smallest distance to road effect was in 2019, with the median value only increasing by 0.065 from 0.075 to 0.140 in the first 25 m. In general, the NDMI was higher in 2016–2017, compared to the other years.

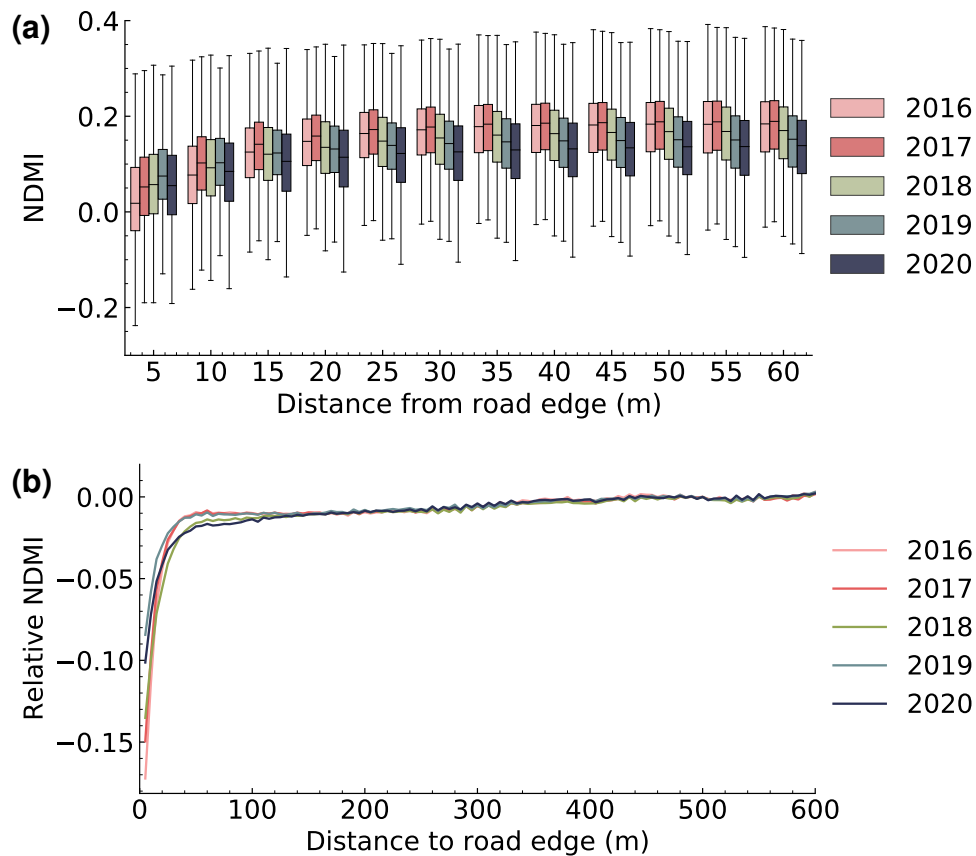


**Figure 3.5:** Temporal and spatial changes in NDMI with distance from the road edge extracted from Sentinel-2 imagery. The year 2016 marks the period of highway construction, and the year 2017 represents the official opening of the highway. The years 2018-2020 represent the periods after construction. (a) shows the distribution of all absolute NDMI values with distance during the period July–August. (b) shows the relative NDMI median values normalized on a distance of 500 m where I assume minor road effects.

To focus on only the road effect of NDMI, I normalized the median results using the NDMI medium values from 500 m away. At this distance, I expected no or only minor effect of the road. The result of the normalized median values is shown in Fig. 3.5b. Substantial differences in NDMI compared to the undisturbed region occur within distances of 25 m from the road edge. However, a notable decrease in NDMI for the years 2018 and 2020 becomes visible at the distance 140 m in the road direction. Within the distances 25 m to 140 m, 2018 and 2020 exhibit a decrease of 0.02 and 0.017 in road direction, respectively, whereas for 2016, 2017 and 2019, the decrease ranges between 0.009 to 0.01.

While the NDMI represents moisture within the vegetation canopy, I was also interested in open water. The road construction can potentially lead to ponding in poorly drained areas along the embankment. First, I calculated the median NIR reflectance of each year. Then, I included all pixels for the year between the road edge and 20 m distance, which were below the water threshold at least once in the time series. Moreover, the pixels are divided into upstream and downstream parts. Since I used the absolute reflectance values for the NIR, no interannual comparison between decrease or increase can be achieved but rather the annual differences between up- and downstream within single years. The result is shown in Fig. 3.6. The year 2016 exhibited lower median values of NIR reflectance on the upstream side, indicating wetter conditions there. However, the following years show generally lower NIR reflectance on the downstream side. The differences between the median are more significant for 2018–2019, compared to the year during construction (2016) and the year of inauguration (2017). The smallest difference between the upstream and downstream median NIR reflectance is observed in 2017, with the upstream median of 0.130 and the downstream median of 0.118, giving a difference of 0.012. In contrast, the most significant difference between the two sides was in 2018, showing an upstream median of 0.13 and a downstream median of 0.09, giving a difference of 0.04 in median NIR reflectance. Further, as shown by the IQR, the variation of NIR reflectance shows a larger variation for the downstream than the upstream side in 2016. In the following years, the variation remains high for both sides. Inter-annual comparison is not possible due to the methods chosen. However, it is worth noting that a general trend towards wetter conditions is indicated on the downstream side compared to a slightly positive trend towards drier conditions on the upstream side.



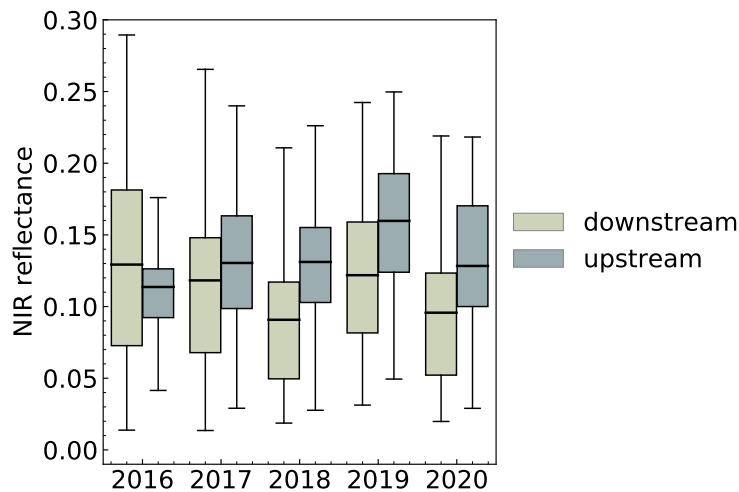


**Figure 3.6:** Distribution of NIR reflectance upstream and downstream of the ITH.

### 3.3 Snow Melt

The presence of snow with distance from ITH is illustrated in Fig. 3.7. Generally, all years show less snow cover closer to the road, including the years before construction (2002 and 2013). However, the size of this effect differs between the time before construction and other years. The years 2002 and 2013 show an even snow cover of the study area of 80% and 10%, respectively. The shape of the graphs for these years are almost identical despite the differences in snow cover. A gradual decrease towards the (at that time not yet constructed) road of approximately 5% snow cover is observed at distances starting at 100 m from the road for both years. Furthermore, the graph of the year 2015, which represents the beginning of the road construction, has a similar shape as the ones before construction.

The snowmelt pattern of 2017, 2018 and 2020 are similar, both in shape and snow cover. For these years, the snow cover increase from 5% in road vicinity to about 20% ( $\pm 5\%$ ) at a distance of 140 m from the road edge. At distances beyond 140 m, there is a gradual increase from 20% ( $\pm 5\%$ ) to 30% ( $\pm 5\%$ ) of snow cover until a distance of 500 m from the road edge where the snow cover stabilizes.

A pronounced decline in snow cover with decreasing distance from road occurred in 2019, with 15% of the area snow-covered in the vicinity of the highway, then drastically increasing for 150 m and stabilizing at 200 m with a snow cover of about 80%. The year 2016 shows the most significant differences in snow cover. The snow cover in the vicinity of the road reaches 6%, and then it increases to 80% following a logarithmic curve up to a distance of 500 m.

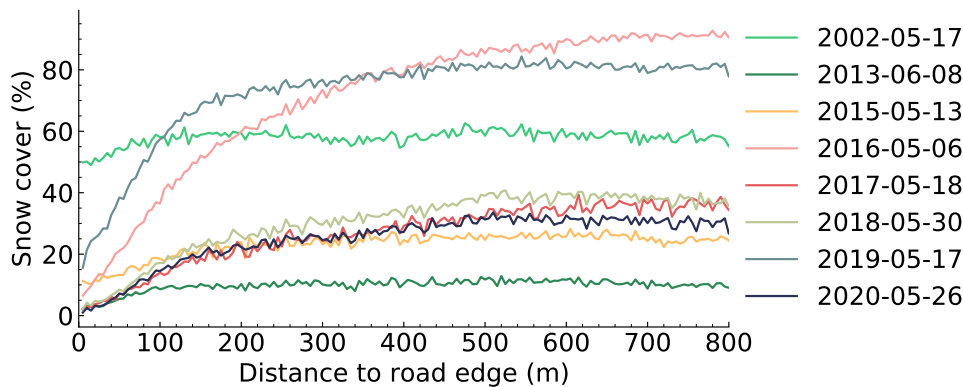


**Figure 3.7:** Presence of snow with distance from ITH derived from Landsat-8 and -7 images using NDSI.

### 3.4 Vegetation Greenness

I examined the vegetation greenness along the road with means of the maximum NDVI for each pixel in the peak of the growing season derived for the years 2016–2020 from Sentinel-2 images. To analyze the distance to road effect, I grouped the pixel values in 5 m buffers from the road. The result is presented in Fig. 3.8. All years show a significant decrease in NDVI towards the road starting approximate 25 m from the road edge. At distances further away, there are no significant changes. The most significant differences in NDVI the first 25 m is observed in 2016. In this year, the median value increased by 0.159 from 0.617 at 5 m to 0.776 at 25 m. The distance to road effect became smaller throughout the years. The year 2020 shows the smallest distance to road effect, with the median value only increasing by 0.103 (from 0.635 to 0.738) in the first 25 m. Overall, the greatest NDVI variation as represented by the IQR in Fig. 3.8 is found 5 m from the road, during construction and the year of opening (2017). At 10 m distance, 2016 and 2017 show a larger variation of NDVI compared to distances further away.

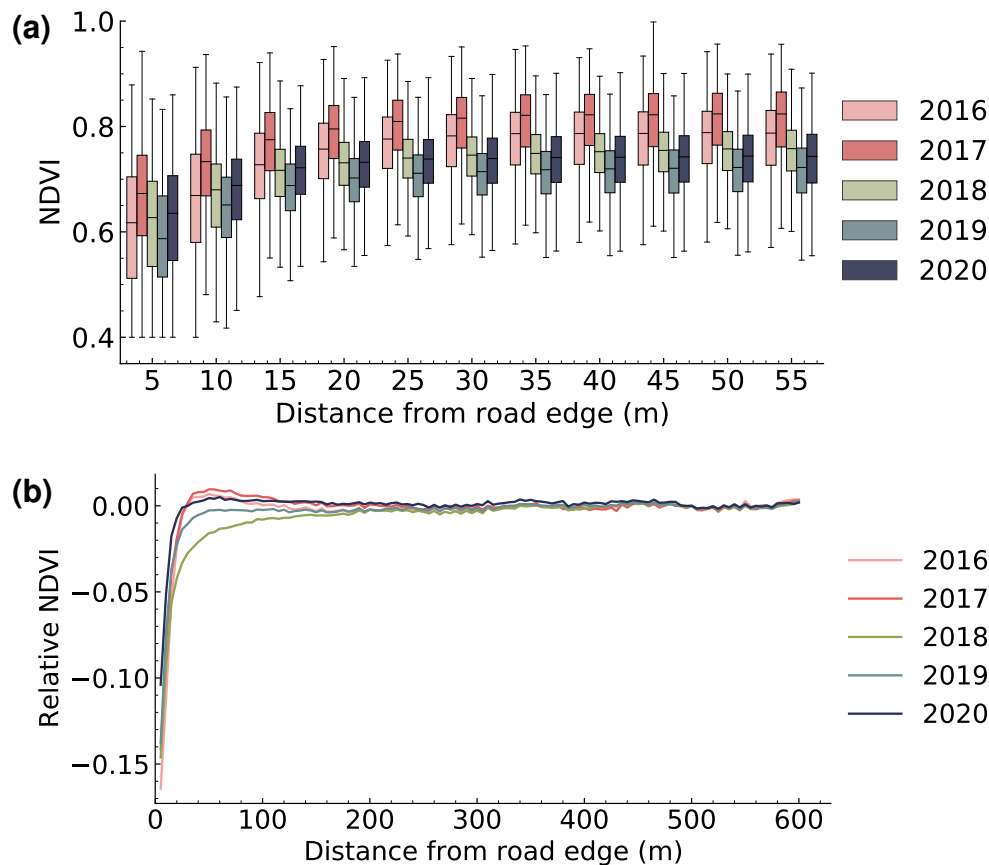


**Figure 3.8:** Distribution of NDVI with distance from the road extracted from Sentinel-2 imagery. The year 2016 represents the period during the highway construction and the year 2017 when the highway was officially opened. The years 2018–2020 represent the periods after construction. (a) shows the maximum NDVI values for each pixel during the period July–August. (b) shows the median NDVI per distance normalized at a distance of 500 m

In addition, I normalized the median NDVI on the distance 500 m which I assumed to be undisturbed by the road, to only concentrate on the road effect (Fig. 3.8b). At distances far from the road, the median NDVI is similar to the 500 m zone for all years. However, at 200 m the NDVI graphs begin to show an observable diverging pattern towards the road before the drastic decrease at 25 m. The pattern is a consequence of some years exhibiting an increase in NDVI and others showing a drop in NDVI, compared to the undisturbed zone. The years 2016 and 2017 show a gradual increase in NDVI, becoming visible at 140 m until it reaches its maximum at approximate 50 m from the road edge. The NDVI in 2019 and 2020 remains rather consistent throughout the distances

far away and shows a negative difference compared to the undisturbed zone at distances closer than 25 m. The year 2018 shows a gradual decrease in NDVI towards the road compared to the undisturbed zone, observable from distances 200 m towards the road. Compared to the undisturbed zone, 2018 shows a decrease of 0.033 at 25 m.

The spatial pattern of NDVI in the vicinity of a road segment shows no significant visual changes when comparing the maximum NDVI values for the peak of the growing season for the years 2016 and 2020 (Fig. 3.9). However, the extent of low NDVI values in the absolute vicinity of the road is larger in 2016 as the construction impact was more intense than in 2020.

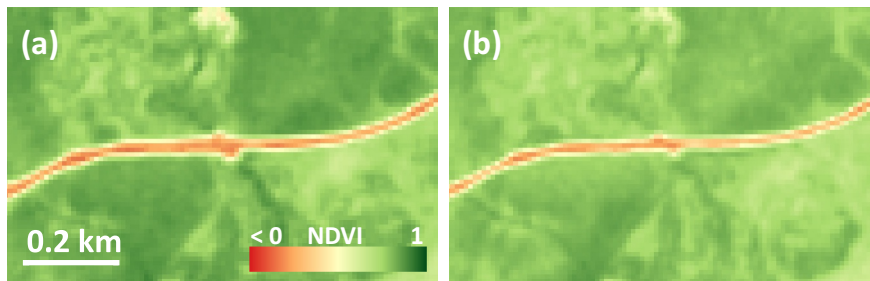


**Figure 3.9:** Maximum NDVI values for the peak of the growing season for a road segment in (a) 2016 and (b) 2020

# 4

## Discussion

### 4.1 Snow Accumulation

In this work, I used a snow-free and a snow-covered ALS dataset to derive snow depths along the ITH (Fig. 3.1). Whereas manual measurements of snow depth are expensive, tedious [76] and limited to the transects or points measured, the indirect measurement of the surface using remote-sensing technologies has the benefits of (I) being non-destructive to the snowpack, (II) being safe for crew members, and (III) enabling to capture the natural variability of snow distribution in areas that are vast and inaccessible. However, usually manually obtained ground truth points are utilized to validate the snow depths obtained using remote sensing methods [77]. Our snow-covered dataset had no available validation points. However, the road could act as ground truth since I assumed that it was snow-free during the data collection. Visual inspection of the transects of snow-covered and snow-free DEM revealed an almost perfect alignment between the two datasets, requiring no further co-registration (Fig. 3.2).

As I hypothesized, snow depths were larger at both sides of the embankment, compared to the surrounding terrain as shown in Fig. 3.3 and Fig. 3.4. This result is in line with similar studies (e.g. [8, 9]). Neill et al. [9] manually measured the snow depths along transects in tundra and forest at the Peel Plateau along with the Dempster Highway (Northwest Territories) and found an enhanced snow accumulation at the embankment in the tundra landscape. They noted a significant enhancement between about 5 and 15 m from the side of the road and then a decrease. However, they did not mention any distances from which the snow depths gradually started to increase. The rather small number of transects (six) and measurements only every 2 m at distances further away than 15 m and no differentiation between the sides of the road might make it hard to observe any gradual increase of snow depths. The

spatially continuous snow-depths presented in this work made it possible to create multiple (more than 3000) transects. In this way, I showed that a gradual increase of snow accumulation could start as far as 36 m away from the road center. The width of the embankment, on the other hand, may have an impact on how far from the road center the snow accumulates. Therefore, this study would benefit from further classification of the snow accumulation depending on the embankment width.

There can be a significant difference in snow accumulation depending on the cardinal direction of the transects, from which I derived the snow-depths (compare Fig. 3.3a-b and Fig. 3.4a-b). Wind and topography could explain the differences of snow accumulation in transect direction because their interaction has a considerable impact on the snow distribution [78]. The embankment may initiate the snow accumulation enhancement, acting as an obstruction in the terrain favoring snow accumulation on the sides of the embankment. A road located perpendicular to the predominant wind direction [8] can favor snow accumulation on the lee side of the embankment. Likewise, less snow accumulates when the road is located parallel to the predominant wind [78].

The average wind directions and speed for Trail Valley Creek research station, which is located close to the study region, are shown in Fig. 4.1. The figure illustrates the period October-December of 2018 and January-April in 2019. This period represents the winter months before AWI acquired the data. The predominant wind direction is south. Based on the findings of [8, 78] and the prevailing southern winds, we should see a significant large snow accumulation for the transects located in north direction compared to in south direction. This is confirmed when comparing the figures in Fig. 3.3. The transects in north direction (leeward side) (Fig. 3.3a) show, as expected, a more enhanced snow accumulation than the southern side (Fig. 3.3b). In the east-west direction, the frequency and average wind speed are similar (Fig. 4.1). The similar frequency and wind speed are also reflected in the snow accumulation for the transects in east-west direction, which look similar in snow depths (compare Fig. 3.4a-b). However, for the transects in west direction, the snow accumulation reaches distances further away from the road center (Fig. 3.4b). A possible explanation might be that many of the transects in west direction are located on a downward slope towards the road (e.g. Fig. 3.2c). On a distance of 75 m from the road, there is a more than 2 m decrease in elevation before

the sudden change in slope due to the embankment appears, which may cause turbulence and snow deposition. Another contributing factor to the snow accumulation is snow plowing which may explain why the accumulation appears on both sides.

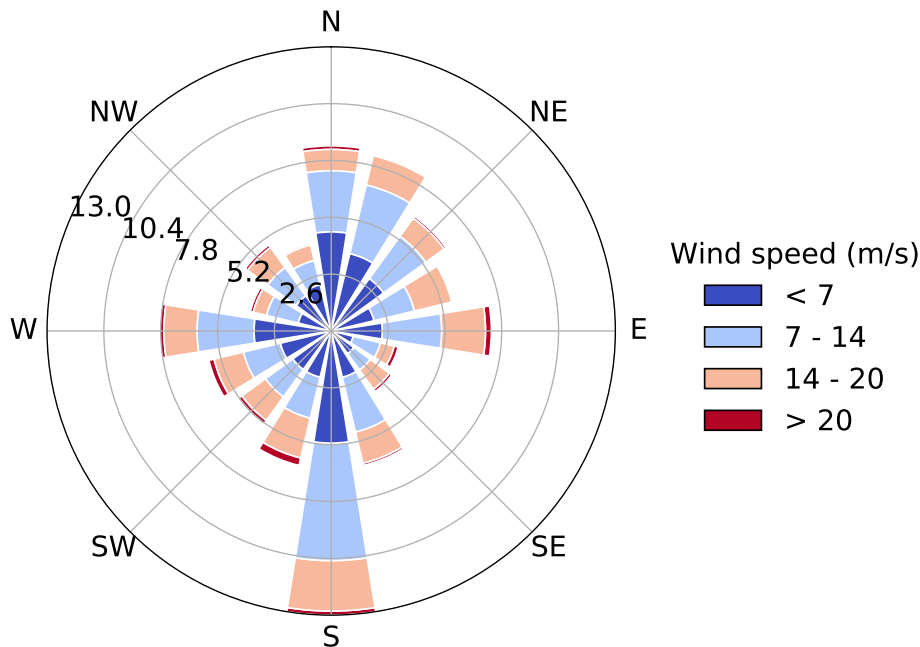


**Figure 4.1:** Wind rose for Trail Valley Creek for the months October-December of 2018 and January-April in 2019 shown in average wind speed in m/s and direction. The predominant winds come from the south for the studied time period.

It should be noted that the results only represent a small section of the road. At sites with lower embankment the snow accumulation may be less pronounced because the lower embankment allows the wind to move in a laminar flow blowing the snow away [79]. Furthermore, the snow accumulation along the embankment is likely less enhanced where there are more trees as they act as a shelter preventing the snow from drifting away as concluded in [9]. Notwithstanding the data coverage limitations, these results give us a better understanding of the spatial distribution of snow next to a permafrost road embankment.

While snow accumulation next to water ponding was identified as one of the key factors contributing to permafrost degradation and increased thaw depths along with infrastructures [13, 14], recent studies have underlined the need to capture high spatial resolution components when modeling infrastructure ele-

ments [14]. Knowing that the spatial pattern of snow remains stable from year to year [80], the map of snow distribution and snow depths could be incorporated into permafrost degradation models and contribute to their validation and improvement.

## 4.2 Vegetation Moisture Content and Surface Water

I used two remote sensing indices (NDMI and NIR) to examine the hypothesized increase in vegetation moisture and wetting of the surface next to the road. In contrast to what I expected, a decrease in NDMI was observed at distances close to the road (Fig. 3.5), indicating a decrease and no increase in vegetation moisture there. However, this finding is in line with other studies using the NDMI to examine the road or infrastructure effect on the vegetation moisture in permafrost. Yu et al. [15] used Landsat-derived indices and observed that the mean NDMI at distances close to the infrastructure was 0.2 ( $\pm 0.02$ ) lower than in undisturbed zones. Further, they observed that the greatest changes occurred within a 100 m zone. Also, [81] showed a substantial drop in NDMI following a permafrost highway construction within the first 100 m from the road.

The decline in NDMI could be attributable to vegetation near the route being killed by excessive levels of road dust [26] or a reduction of total biomass and species richness as shown in [23]. However, studies have also demonstrated that infrastructure on permafrost promotes the growth of shrubs [23, 26, 28] and graminoid populations [23]. Therefore, it is likely that the deposition of dust influences the spectral response of NDMI. The spectral bands used for the calculation of the NDMI are the NIR and SWIR with wavelength ranges of 1.54  $\mu\text{m}$  to 1.68  $\mu\text{m}$  and 0.77  $\mu\text{m}$  to 0.91  $\mu\text{m}$ , respectively. Ackerman and Finlay [28] showed that dust deposition on leaves increased the reflectance throughout the 0.4  $\mu\text{m}$  to 0.7  $\mu\text{m}$  photosynthetically active wavelength range. NIR, however, did not show any significant changes, and hence the investigated NDVI was reduced with dust deposition. However, their study was limited to wavelengths smaller than 1.130  $\mu\text{m}$  and did not include SWIR. Future studies could use other spectral indices such as NDMI to investigate the response to dust deposition. Moreover, the contribution of the mixed pixels to the resulting



---

NDMI should not be neglected (further discussed in section 4.4).

For the wetting of the surface, I utilized the NIR band of the Sentinel-2 using a buffer of 20 m around the road. An important source of error for this small scale analysis is the workflow being carried out on fixed distances from buffers along a vectorized road derived from one Sentinel-2 image in 2016. Co-registration of the images was performed in a pre-processing step, however slight offsets could not be removed completely in order to achieve a perfect spatial alignment of each pixel. Therefore, a dynamic distance calculation for each pixel to the road for each image could improve the results.

The decision to use a single-band water index rather than the standard open water delineation multi-band index NDWI as suggested by [61] was the poor performance of the NDWI in detecting smaller water ponds along the road. I attributed the poor performance of NDWI to shallow water bodies with bottom reflectance and turbidity [62]. The application of NIR reflectance in mapping open water bodies has achieved equivalent or even better results than other common water indices [82] because of the substantial absorption of incoming NIR irradiation by water. The limitation in using a single band index is generally the threshold. Whereas a multi-band index has the benefit of an optimal threshold that can be utilized on satellite imagery from different sensors and regions, a new optimal threshold for each image might be required to obtain the highest accuracy for a single band index as NIR [82]. However, NIR showed the highest contrast between water and non-water bodies and an optimum threshold of 0.128 exhibited the highest accuracy over other water indices [64]. As a result, I employed the same threshold in this work with the caveat that the region's optimal threshold might differ from theirs. Visual inspections of the images utilizing the threshold, on the other hand, revealed good performance. I calculated the median NIR value for each pixel and year. In the annual time series, I preserved every pixel that had values equal to or less than the threshold at least once throughout the time series (Fig. 2.12).

Due to differences in illumination, acquisition geometry, as well as sensor spectroradiometry [62], I compared the distribution of the NIR reflectance values between the upstream and downstream side in each year instead of the absolute values. The findings revealed that disparities in NIR median reflectance tend to increase with time. Unlike suggested water ponding on the upstream

side [15–17], I found indications of wetter conditions on the downstream side all years except 2016. A possible explanation for the discrepancy to previous studies might be the period I studied (July and August). Winter streamflow is increasing in Northwest Territories [83] and if the stream reaches the culvert, possible clogging due to aufeis [17] can contribute to upstream ponding in spring and early summer. Later in summer, the pond may exhibit rapid drainage through the culvert as the aufeis melts. The fast flow may cause local erosion downstream, favoring a possible pond formation there. In order to detect water ponding on the upstream side caused by winter streamflow and evaluate if there is a transition between upstream and downstream ponding in the summer, the study could benefit from incorporating acquisitions from the spring and early summer. Only in 2016, the upstream side exhibited lower values than the downstream side. The wetter conditions in 2016 imply that standing water had already increased before road opening in 2017. This finding is in agreement with the study of Reynolds et al. [26] who showed the development of water ponds shortly after gravel road construction at the Prudhoe Bay Oilfield in northern Alaska. Additionally, culverts may not have been installed in all areas along the road where they were required, resulting in water ponding in such an early stage. Future research could benefit from incorporating photos taken before construction to track the evolution from the beginning. This could be achieved by using a combination of Landsat-8 and Sentinel-2. In Arctic-Boreal permafrost regions, a spectral comparison of Landsat-8 and Sentinel-2 comparable bands revealed that the two sensors correlate well and portray similar trends with just slight deviations [84]. The panchromatic band in Landsat or other high-resolution imagery could be used to pan-sharpen the images [63, 85] in order to obtain a common resolution.

### 4.3 Snow Melt

I examined the snowmelt patterns along the road using NDSI derived from Landsat data. Even though snow accumulates near the road as shown in the section 3.1, these areas are melting earlier than regions further away in spring (Fig. 3.7). The results are in line with the hypothesis that snow melts earlier in the vicinity of the road. However, most of the additional snow accumulation is within 30 m (Fig. 3.3 and 3.4), which is also the spatial resolution of the Landsat bands used for calculating the NDSI. Therefore, even if the snow in the absolute vicinity of the road persists longer because of the large snow

depths, it may not be visible in the images because of the spatial resolution of the utilized sensor.

Other studies have identified road dust as the main cause for the early melt-off in spring [21, 22]. Dust loading on snow leads to decreased albedo and, thus, increased solar energy, inducing snowmelt. Everett et al. [22] showed that most dust falls within a distance of 300 m with a logarithmic decrease. This finding is in accordance with the spatial pattern of snowmelt found in this work, especially for 2016 and 2019, representing a high snow cover further away from the road (90% and 80%, respectively).

The extent of the early snowmelt is larger in this work compared to other studies. The main snowmelt extent in this work was within a zone of 150 m whereas Walker et al. [21] noted that the early snowmelt occurred primarily within a 100 m zone. The most obvious explanation for the differences in snowmelt is the misclassification of the NDSI when the snow is contaminated with dust and thus falsely classified as snow-free. However, the reliability of the NDSI given different spectral characteristics of the snow was examined in [86]. They found that the NDSI values for all types of snow, such as fresh, clean, patchy and wet, and contaminated were substantially different than snow-free areas. Other explanations for the differences in snowmelt extent might be different wind speed, dust particle size and snow clearance practices.

The early melt-off has many possible consequences for the permafrost. Auerbach et al. [23] found the deepest thaw depth next to the Dalton Highway (Alaska) and a consistent decrease with distance from the road. They attributed the increased thaw depth close to the road to the earlier exposure to solar radiation. The melt-off can start up to 14 days before the general melt-off [21], which can affect the underlying vegetation. The vegetation phenology and start of the season are significantly correlated with the last day of snow cover as found in [87]. Some plants might be more favored by early snowmelt than others, as noted in [23]. They highlighted the close relationship between early snowmelt and vascular plant growth, deciduous shrub and sedge flowering. Tall shrubs may act as a windbreak, increasing dust deposition and snow accumulation, leading to more soil nutrients, higher soil temperatures and increased active layer thickness [24]. My results indicate that dust deposition is the main driver of the early snowmelt and more attention should be paid

---

to further research on the extent of dust deposition along the road and the performance of NDSI on snow contaminated with dust. As the early snowmelt impacts the underlying permafrost in various ways and might be initiated by dust deposition, the incorporation of field measurements is needed for validating the remotely sensed estimations of snowmelt. Moreover, the NDSI may be implemented in machine learning algorithms to detect dust deposition on the surrounding vegetation together with the NDVI, which already has been shown to be influenced by dust [28].

## 4.4 Vegetation Greenness

Gravel roads constructed on permafrost contribute to substantial changes in the vegetation alongside the route [24, 26, 28]. For example, changes in vegetation can be induced by increased soil nutrient availability, following a dust deposition, and an elevated soil moisture [24]. Based on this knowledge, I hypothesized that the amounts of green vegetation would be promoted in the vicinity of the road and increase the NDVI. Another possible reason for altered vegetation is the disturbance along the swath next to the embankment during construction, which can also promote shrub recruitment [88]. The method to analyze these changes relied on the NDVI calculated from Sentinel-2 images starting from the year 2016 when the road was still under construction. As can be seen on the photos from September 21, 2021 (Fig. 4.2), the vegetation is altered to a distance of a couple of meters from the road. Surprisingly, the results presented in Fig. 3.8a-b show a decrease in NDVI towards the road, starting at a distance of 25 m from the road edge. Indeed, the same spatial pattern was seen in [15] where Landsat images and buffer zones from an oil and gas disturbance were used in a region with discontinuous permafrost in northwestern Siberia. The NDVI in that study showed very low values within a 100 m distance from the disturbance, and past that range, there was no substantial difference. In this work, I normalized the median NDVI values on distances 500 m away from the road edge (Fig. 3.8b). I considered regions beyond that distance as undisturbed. With means of the normalization, I could show an effect beginning as much as 200 m from the road edge before the drastic decrease around 25 m. Because of the notable spatial pattern occurring, with some years showing a decrease in the median NDVI, whereas others were showing an increase, the pattern should be considered as an independent effect irrespective to the common drastic decrease at 25 m. The effect can not

be explained by the earlier snowmelt onset as shown in section 3.3, since the snow melts earlier the closer to the road for all years. Thus an earlier onset of greening in the vicinity of the road should be valid for all years and not only 2016 and 2017.



**Figure 4.2:** Photos of a segment of the ITH and the adjacent vegetation (from 21 September 2021). Photo credits: Boike, J.

Due to the finer spatial resolution for the NIR and red band of Sentinel-2 (10 m), compared to Landsat with 30 m, I chose to utilize the Sentinel-2. However, if the vegetation change is limited to only a few meters from the road, even the spatial resolution of 10 m may not be sufficient to record these changes. The mixed pixels next to the road can be compiled partly from vegetation with larger positive NDVI values and the road, typically having NDVI values lower than 0.1. In this case, the NDVI values are not representative. Another possible reason for the negative effect of the road on vegetation greenness may be the time it takes for altered vegetation to exceed the size of a Sentinel-2 pixel. At the Dempster Highway (Northwest Territories), which has been in operation since the late seventies, a shrub profligation has been shown within the first 100 m from the road [24]. Because ITH has been operational since 2017, it may be too early to notice any changes using medium-resolution satellite photography. Furthermore, the lower NDVI-values closer to the road might be influenced by the dust deposition from the road. Deposited dust might kill the vegetation [26] or block the spectral characteristics of the underlying leaf surface, reducing the NDVI by as much as 0.24 as shown in [28]. At the Dalton highway, located in Alaska, NDVI-values were reduced up to a distance of 125 m and after dust removal, the NDVI-values were stable at all distances.

Moreover, heavy machinery operating laterally at the embankment can kill vegetation giving a lower NDVI-value during the construction. However, these microsites may be favored for shrub recruitment in the future [88], and therefore, show higher NDVI values with time. An indication for the development of microsites is revealed when comparing the Fig. 3.9a-b. There is a significant difference in NDVI between the years in road proximity. The spatial extent of low NDVI values is much more prominent in 2016 than 2020. In 2020, the vegetation along the road appeared to have recovered throughout the years. Fig. 4.2 also indicates that a secondary succession might have promoted the growth of pioneering species such as grasses [23].

# 5

## Conclusion

In this work, I aimed to examine potential drivers of permafrost degradation along the ITH using remote sensing techniques. Based on the current knowledge, I identified potential permafrost degradation drivers that additionally can be investigated via remote sensing. I followed the hypotheses (I) snow accumulates next to the embankment toe (II) vegetation moisture content and surface water increase in poorly drained areas along the embankment toe (III) snow melts earlier in the vicinity of the highway and (IV) vegetation greenness increase along the road.

I can conclude that an effect of the road is observed in all physical parameters. However, the effect in the result is sometimes inconsistent with the hypotheses. For instance, the results show a significant decrease in NDVI and NDMI at close distances from the road, indicating a decrease instead of the hypothesized increase in vegetation greenness and moisture. Furthermore, the comparison of NIR reflectance as an indicator of wetting shows an increase of wetter conditions on the downstream side rather than the upstream. Meanwhile, the results reveal agreement in the hypothesized snow accumulation along the embankment and earlier snowmelt, reaching up to distances 500 m from the road edge.

As much as remote sensing delivers many possibilities to study vast regions with high spatial coverage and a high temporal resolution, caution is recommended when interpreting the results of a gravel road's effect on permafrost. This is especially relevant when examining multi-spectral indices, which may be biased because of other factors, such as dust. Dust is not explicitly accounted for in this work but seems to impact all parameters. Therefore, future studies could focus on retrieving information about the dust load in the adjacent road regions with the help of satellite sensor signals.

ITH provides an opportunity to document how infrastructure affects permafrost from the beginning. Remote sensing can serve as baseline data. However, it needs to be accounted for the limitations e.g. mixed pixels and spectral block because of dust. Further, when utilizing medium resolution satellite data, the road's relatively young age becomes a limiting factor, as the changes of the physical parameters are unlikely to have exceeded the spatial scale of the data in such a short time. Therefore, applying the utilized methods and data types on a permafrost road that has been in use for a more extended period with confirmed changes in the selected parameters would be beneficial. This would help to validate the impact of the road and add more knowledge to the potential to identify permafrost degradation drivers with remote sensing techniques. Due to the utilization of cloud computing services, open-source software packages, and freely available datasets (except the ALS dataset), the methods are highly reproducible and can easily be transferred to another study region.

Overall, primarily free available remote sensing data has been utilized for the first time over the ITH in order to examine permafrost degradation drivers. The research identifies the limitations of specific physical parameters and the parameters that are best studied via remote sensing and lays the ground for future road monitoring.



# Bibliography

- [1] B. K. Biskaborn, S. L. Smith, J. Noetzli, H. Matthes, G. Vieira, D. A. Streletskiy, P. Schoeneich, V. E. Romanovsky, A. G. Lewkowicz, A. Abramov, M. Allard, J. Boike, W. L. Cable, H. H. Christiansen, R. Delaloye, B. Diekmann, D. Drozdov, B. Etzelmüller, G. Grosse, M. Guglielmin, T. Ingeman-Nielsen, K. Isaksen, M. Ishikawa, M. Johansson, H. Johansson, A. Joo, D. Kaverin, A. Kholodov, P. Konstantinov, T. Kröger, C. Lambiel, J. P. Lanckman, D. Luo, G. Malkova, I. Meiklejohn, N. Moskalenko, M. Oliva, M. Phillips, M. Ramos, A. B. K. Sannel, D. Sergeev, C. Seybold, P. Skryabin, A. Vasiliev, Q. Wu, K. Yoshikawa, M. Zheleznyak, and H. Lantuit. “Permafrost is warming at a global scale”. *Nature Communications* 10:1 (2019), pp. 1–11. DOI: 10.1038/s41467-018-08240-4 (see page 1).
- [2] S. Harris. “The alpine periglacial Zone”. In: *Advances in Periglacial Geomorphology*. Ed. by M. J. Clark. Publisher: John Wiley and Sons Ltd, 1988. Chap. 15, pp. 369–413 (see page 1).
- [3] J. Obu, S. Westermann, A. Bartsch, N. Berdnikov, H. H. Christiansen, A. Dashtseren, R. Delaloye, B. Elberling, B. Etzelmüller, A. Kholodov, A. Khomutov, A. Kääb, M. O. Leibman, A. G. Lewkowicz, S. K. Panda, V. Romanovsky, R. G. Way, A. Westergaard-Nielsen, T. Wu, J. Yamkhin, and D. Zou. “Northern Hemisphere permafrost map based on TTOP modelling for 2000–2016 at 1km<sup>2</sup> scale”. *Earth-Science Reviews* 193 (2019), pp. 299–316. DOI: <https://doi.org/10.1016/j.earscirev.2019.04.023> (see page 1).
- [4] S. Westermann, C. R. Duguay, G. Grosse, and A. Kääb. “Remote sensing of permafrost and frozen ground”. *Remote Sensing of the Cryosphere*: January 2015 (2014), pp. 307–344. DOI: 10.1002/9781118368909.ch13 (see page 1).

- [5] N. I. Shiklomanov, D. A. Streletskiy, J. D. Little, and F. E. Nelson. “Isotropic thaw subsidence in undisturbed permafrost landscapes”. *Geophysical Research Letters* 40:24 (2013), pp. 6356–6361. DOI: 10.1002/2013GL058295 (see page 1).
- [6] F. E. Nelson, O. A. Anisimov, and N. I. Shiklomanov. “Subsidence risk from thawing permafrost”. *Nature* 410:6831 (2001), pp. 889–890. DOI: 10.1038/35073746 (see page 1).
- [7] Government of Canada. *Infrastructure Canada Projects and Programs (since 2002) - Northwest Territories*. URL: <https://www.infrastructure.gc.ca/investments-2002-investissements/nt-eng.html>. Accessed: 2021-08-15 (see page 1).
- [8] C. Benson, B. Holmgren, R. Timmer, G. Weller, and S. Parrish. “Observations on the seasonal snow cover and radiation climate at Prudhoe Bay, Alaska during 1972”. *Ecological investigations of the tundra biome in the Prudhoe Bay region, Alaska. Biological Papers of the University of Alaska, Special report: 2* (1975), pp. 12–50 (see pages 1, 39, 40).
- [9] H. B. O. Neill and C. R. Burn. “Impacts of variations in snow cover on permafrost stability, including simulated snow management, Dempster Highway, Peel Plateau, Northwest Territories”. *Arctic Science* 3 (2017), pp. 150–178. DOI: [dx.doi.org/10.1139/as-2016-0036](https://doi.org/10.1139/as-2016-0036) (see pages 1, 39, 41).
- [10] T. Zhang. “Influence of the seasonal snow cover on the ground thermal regime: An overview”. *Reviews of Geophysics* 43:4 (2005). DOI: 10.1029/2004RG000157 (see pages 1, 2).
- [11] M. M. Darrow. “Thermal modeling of roadway embankments over permafrost”. *Cold Regions Science and Technology* 65:3 (2011), pp. 474–487. DOI: 10.1016/j.coldregions.2010.11.001 (see page 2).
- [12] Y. Ge and G. Gong. “Land surface insulation response to snow depth variability”. *Journal of Geophysical Research Atmospheres* 115:8 (2010), pp. 1–11. DOI: 10.1029/2009JD012798 (see pages 2, 4).
- [13] H. Park, A. N. Fedorov, M. N. Zheleznyak, P. Y. Konstantinov, and J. E. Walsh. “Effect of snow cover on pan-Arctic permafrost thermal regimes”. *Climate Dynamics* 44:9-10 (2015), pp. 2873–2895. DOI: 10.1007/s00382-014-2356-5 (see pages 2, 4, 41).

- [14] T. Schneider von Deimling, H. Lee, T. Ingeman-Nielsen, S. Westermann, V. Romanovsky, S. Lamoureux, D. A. Walker, S. Chadburn, E. Trochim, L. Cai, J. Nitzbon, S. Jacobi, and M. Langer. “Consequences of permafrost degradation for Arctic infrastructure – bridging the model gap between regional and engineering scales”. *The Cryosphere* 15:5 (2021), pp. 2451–2471. DOI: 10.5194/tc-15-2451-2021 (see pages 2, 4, 41, 42).
- [15] Q. Yu, H. E. Epstein, R. Engstrom, N. Shiklomanov, and D. Streletskiy. “Land cover and land use changes in the oil and gas regions of Northwestern Siberia under changing climatic conditions”. *Environmental Research Letters* 10:12 (2015). DOI: 10.1088/1748-9326/10/12/124020 (see pages 2–4, 12, 20, 42, 44, 46).
- [16] R. Berg. “Road performance and associated investigations”. In: *Environmental engineering and ecological baseline investigations along the Yukon River-Prudhoe Bay Haul Road*. Ed. by J. Brown and R. Berg. Publisher: U.S. Army Cold Regions Research and Engineering Laboratory, 1980. Chap. 3, pp. 53–91 (see pages 2, 4, 44).
- [17] T. Ensom, O. Makarieva, P. Morse, D. Kane, V. Alekseev, and P. Marsh. “The distribution and dynamics of aufeis in permafrost regions”. *Permafrost and Periglacial Processes* 31:3 (2020), pp. 383–395. DOI: 10.1002/ppp.2051 (see pages 2, 4, 44).
- [18] I. de Grandpré, D. Fortier, and E. Stephani. “Degradation of permafrost beneath a road embankment enhanced by heat advected in groundwater 1”. *Canadian Journal of Earth Sciences* 49:8 (2012), pp. 953–962. DOI: 10.1139/E2012-018 (see page 2).
- [19] J. van der Sluijs, S. V. Kokelj, R. H. Fraser, J. Tunnicliffe, and D. Lacelle. “Permafrost terrain dynamics and infrastructure impacts revealed by UAV photogrammetry and thermal imaging”. *Remote Sensing* 10:11 (2018). DOI: 10.3390/rs10111734 (see pages 2, 3).
- [20] P. D. Morse and S. A. Wolfe. “Geological and meteorological controls on icing (aufeis) dynamics (1985 to 2014) in subarctic Canada”. *Journal of Geophysical Research: Earth Surface* 120:9 (2015), pp. 1670–1686. DOI: <https://doi.org/10.1002/2015JF003534> (see page 2).
- [21] D. A. Walker and K. R. Everett. “Road dust and its environmental impact on Alaskan taiga and tundra”. *Arctic & Alpine Research* 19:4 (1987), pp. 479–489. DOI: 10.2307/1551414 (see pages 2, 4, 45).

- [22] K. R. Everett. “Distribution and properties of road dust along the northern portion of the Haul Road”. In: *Environmental engineering and ecological baseline investigations along the Yukon River-Prudhoe Bay Haul Road*. Ed. by J. Brown and R. Berg. Publisher: U.S. Army Cold Regions Research and Engineering Laboratory, 1980. Chap. 3, pp. 101–128 (see pages 2, 20, 45).
- [23] N. A. Auerbach, M. D. Walker, and D. A. Walker. “Effects of roadside disturbance on substrate and vegetation properties in arctic tundra”. *Ecological Applications* 7:1 (1997), pp. 218–235. DOI: 10.1890/1051-0761(1997)007[0218:EORDOS]2.0.CO;2 (see pages 2, 42, 45, 48).
- [24] H. K. Gill, T. C. Lantz, B. O’Neill, and S. V. Kokelj. “Cumulative impacts and feedbacks of a gravel road on shrub tundra ecosystems in the Peel Plateau, Northwest Territories, Canada”. *Arctic, Antarctic, and Alpine Research* 46:4 (2014), pp. 947–961. DOI: 10.1657/1938-4246-46.4.947 (see pages 2, 4, 45–47).
- [25] D. Ackerman. “Shrub-induced snowpack variability alters wintertime soil respiration across a simulated tundra landscape”. *Polar Research* 37:1 (2018). DOI: 10.1080/17518369.2018.1468197 (see page 3).
- [26] M. K. Reynolds, D. A. Walker, K. J. Ambrosius, J. Brown, K. R. Everett, M. Kanevskiy, G. P. Kofinas, V. E. Romanovsky, Y. Shur, and P. J. Webber. “Cumulative geocological effects of 62 years of infrastructure and climate change in ice-rich permafrost landscapes, Prudhoe Bay Oilfield, Alaska”. *Global Change Biology* 20:4 (2014), pp. 1211–1224. DOI: 10.1111/gcb.12500 (see pages 3, 42, 44, 46, 47).
- [27] J. Keller and R. Lamprecht. “Road dust as an indicator for air pollution transport and deposition: An application of SPOT imagery”. *Remote Sensing of Environment* 54:1 (1995), pp. 1–12. DOI: 10.1016/0034-4257(95)00119-L (see page 3).
- [28] D. E. Ackerman and J. C. Finlay. “Road dust biases NDVI and alters edaphic properties in Alaskan arctic tundra”. *Scientific Reports* 9:1 (2019), pp. 1–8. DOI: 10.1038/s41598-018-36804-3 (see pages 3, 4, 20, 42, 46, 47).
- [29] *Inuvik Tuktoyaktuk Highway road connecting Canada’s arctic coast*. 2018 (see page 3).

- [30] V. Rampton. *Quaternary Geology of the Tuktoyaktuk Coastlands, Northwest Territories*. Commission géologique du Canada. Memoir. Publisher: Energy, Mines and Resources Canada, 1988. ISBN: 9780660127439. URL: <https://books.google.de/books?id=LqFsnQAACAAJ> (see page 5).
- [31] S. Antonova, C. Thiel, B. Höfle, K. Anders, V. Helm, S. Zwieback, S. Marx, and J. Boike. “Estimating tree height from TanDEM-X data at the northwestern Canadian treeline”. *Remote Sensing of Environment* 231:November 2018 (2019). DOI: 10.1016/j.rse.2019.111251 (see page 5).
- [32] C. R. Burn and S. V. Kokelj. “The environment and permafrost of the Mackenzie Delta area”. *Permafrost and Periglacial Processes* 20:2 (2009), pp. 83–105. DOI: <https://doi.org/10.1002/ppp.655> (see page 5).
- [33] J. Brandt. “The extent of the North American boreal zone”. *Environmental Reviews* 17:NA (2009), pp. 101–161. DOI: 10.1139/A09-004 (see page 6).
- [34] A. Duk-Rodkin and D. Lemmen. “Glacial history of the Mackenzie region”. *Bulletin of the Geological Survey of Canada* 547 (Jan. 2001), pp. 11–20 (see page 6).
- [35] L. Dyke and G. Brooks. “The physical environment of the Mackenzie Valley, Northwest Territories: a base line for the assessment of environmental change. Geological Survey of Canada”. *Bulletin* (Jan. 2000) (see page 7).
- [36] Porter, C. et al. *ArcticDEM*. URL: <https://www.pgc.umn.edu/data/arcticdem/>. Accessed: 2021-12-15. 2018. DOI: <https://doi.org/10.7910/DVN/OHHUKH> (see pages 7, 14).
- [37] Government of Canada. *Historical Climate Data*. URL: <https://climate.weather.gc.ca/>. Accessed: 2021-07-15 (see pages 7, 8).
- [38] S. V. Kokelj, M. J. Palmer, T. C. Lantz, and C. R. Burn. “Ground Temperatures and Permafrost Warming from Forest to Tundra, Tuktoyaktuk Coastlands and Anderson Plain, NWT, Canada”. *Permafrost and Periglacial Processes* 28:3 (2017), pp. 543–551. DOI: 10.1002/ppp.1934 (see page 7).
- [39] Kiggiak - EBA. *Environmental impact statement for construction of the Inuvik to Tuktoyaktuk highway, NWT*. 2011 (see page 8).

- [40] Riegler. *Airborne laser scanner with online waveform processing*. URL: [http://www.riegl.com/uploads/tx\\_pxpriegldownloads/DataSheet\\_VQ-580\\_2015-03-23.pdf](http://www.riegl.com/uploads/tx_pxpriegldownloads/DataSheet_VQ-580_2015-03-23.pdf). Accessed: 2021-10-15 (see page 9).
- [41] S. Hendricks. *AWI ALS toolbox*. URL: <https://github.com/shendric/awi-als-toolbox.git>. Accessed: 2021-08-15. 2019 (see page 9).
- [42] T. J. Pingel, K. C. Clarke, and W. A. McBride. “An improved simple morphological filter for the terrain classification of airborne LIDAR data”. *ISPRS Journal of Photogrammetry and Remote Sensing* 77 (2013), pp. 21–30. DOI: <https://doi.org/10.1016/j.isprsjprs.2012.12.002> (see page 9).
- [43] The European Space Agency. *Sentinel-2 MSI User Guide*. URL: <https://sentinel.esa.int/web/sentinel/user-guides/sentinel-2-msi>. Accessed: 2021-09-15. 2021 (see page 10).
- [44] M. Drusch, U. Del Bello, S. Carlier, O. Colin, V. Fernandez, F. Gascon, B. Hoersch, C. Isola, P. Laberinti, P. Martimort, A. Meygret, F. Spoto, O. Sy, F. Marchese, and P. Bargellini. “Sentinel-2: ESA’s Optical High-Resolution Mission for GMES Operational Services”. *Remote Sensing of Environment* 120 (2012), pp. 25–36. DOI: 10.1016/j.rse.2011.11.026 (see page 10).
- [45] F. Yin, P. Lewis, J. Gomez-Dans, and Q. Wu. “A sensor-invariant atmospheric correction method: application to Sentinel-2/MSI and Landsat 8/OLI” (Feb. 2019). DOI: 10.31223/osf.io/ps957 (see page 13).
- [46] D. Courault, B. Séguin, and A. Olioso. “Review to estimate Evapotranspiration from remote sensing data: some examples from the simplified relationship to the use of mesoscale atmospheric models.” In: 2003 (see page 13).
- [47] E. Vermote, D. Tanre, J. Deuze, M. Herman, and J.-J. Morcette. “Second Simulation of the Satellite Signal in the Solar Spectrum, 6S: an overview”. *IEEE Transactions on Geoscience and Remote Sensing* 35:3 (1997), pp. 675–686. DOI: 10.1109/36.581987 (see page 13).
- [48] R. Wilson. “Py6S: A Python interface to the 6S radiative transfer model”. *Computers & Geosciences* 51 (2013), pp. 166–171. DOI: <https://doi.org/10.1016/j.cageo.2012.08.002> (see page 13).

- [49] S. Murphy. *Github Repository of Sam Murphy*. URL: <https://github.com/samsammurphy/gee-atmcorr-S2>. Accessed: 2021-09-15. 2017 (see pages 13, 14).
- [50] I. Sola, A. García-Martín, L. Sandonís-Pozo, J. Álvarez-Mozos, F. Pérez-Cabello, M. González-Audicana, and R. Montorio Llovería. “Assessment of atmospheric correction methods for Sentinel-2 images in Mediterranean landscapes”. *International Journal of Applied Earth Observation and Geoinformation* 73:February (2018), pp. 63–76. DOI: 10.1016/j.jag.2018.05.020 (see page 13).
- [51] L. Gómez-Chova, G. Camps-Valls, J. Calpe, L. Guanter, and J. Moreno. “Cloud-screening algorithm for ENVISAT/MERIS multispectral images”. *Geoscience and Remote Sensing, IEEE Transactions on* 45 (Jan. 2008), pp. 4105–4118. DOI: 10.1109/TGRS.2007.905312 (see page 15).
- [52] B. N. Duncan, L. E. Ott, J. B. Abshire, L. Brucker, M. L. Carroll, J. Carton, J. C. Comiso, E. P. Dinnat, B. C. Forbes, A. Gonsamo, W. W. Gregg, D. K. Hall, I. Ialongo, R. Jandt, R. A. Kahn, A. Karpechko, S. R. Kawa, S. Kato, T. Kumpula, E. Kyrölä, T. V. Loboda, K. C. McDonald, P. M. Montesano, R. Nassar, C. S. Neigh, C. L. Parkinson, B. Poulter, J. Pulliainen, K. Rautiainen, B. M. Rogers, C. S. Rousseaux, A. J. Soja, N. Steiner, J. Tamminen, P. C. Taylor, M. A. Tzortziou, H. Virta, J. S. Wang, J. D. Watts, D. M. Winker, and D. L. Wu. “Space-Based Observations for Understanding Changes in the Arctic-Boreal Zone”. *Reviews of Geophysics* 58:1 (2020). e2019RG000652 2019RG000652, e2019RG000652. DOI: <https://doi.org/10.1029/2019RG000652> (see page 15).
- [53] A. Zupanc. *Improving Cloud Detection with Machine Learning*. URL: <https://medium.com/sentinel-hub/improving-cloud-detection-with-machine-learning-c09dc5d7cf13>. Accessed: 2021-09-15. 2019 (see page 15).
- [54] A. Zupanc. *Sentinel Hub Cloud Detector*. URL: <https://www.sentinel-hub.com/sites/default/s2cloudless.pdf>. Accessed: 2021-09-15 (see page 15).
- [55] A. Zupanc. *Cloud Masks at Your Service*. URL: <https://medium.com/sentinel-hub/cloud-masks-at-your-service-6e5b2cb2ce8a>. Accessed: 2021-09-15. 2020 (see page 15).
- [56] J. Miceli and J. Braaten. *Sentinel-2 Cloud Masking with s2cloudless*. URL: <https://github.com/google/earthengine-community/tree/master/tutorials/sentinel-2-s2cloudless>. Accessed: 2021-09-15. 2020 (see page 15).

- [57] Earth Resources Observation and Science Center. *Comparison of Landsat 7 and 8 bands with Sentinel-2*. URL: <https://www.usgs.gov/media/images/comparison-landsat-7-and-8-bands-sentinel-2>. Accessed: 2022-01-05. 2015 (see page 16).
- [58] B.-c. Gao. “NDWI—A normalized difference water index for remote sensing of vegetation liquid water from space”. *Remote Sensing of Environment* 58:3 (1996), pp. 257–266. DOI: [https://doi.org/10.1016/S0034-4257\(96\)00067-3](https://doi.org/10.1016/S0034-4257(96)00067-3) (see page 17).
- [59] sentinel-hub. *Normalized Difference Moisture Index (NDMI)*. URL: <https://custom-scripts.sentinel-hub.com/custom-scripts/sentinel-2/ndmi/>. Accessed: 2021-09-15 (see page 17).
- [60] Earth Observing System. *NDMI (Normalized Difference Moisture Index)*. URL: <https://eos.com/make-an-analysis/ndmi/>. Accessed: 2021-12-15. 2022 (see page 17).
- [61] S. K. McFeeters. “The use of the Normalized Difference Water Index (NDWI) in the delineation of open water features”. *International Journal of Remote Sensing* 17:7 (1996), pp. 1425–1432. DOI: 10.1080/01431169608948714 (see pages 17, 43).
- [62] S. Muster, B. Heim, A. Abnizova, and J. Boike. “Water body distributions across scales: A remote sensing based comparison of three arctic tundra wetlands”. *Remote Sensing* 5:4 (2013), pp. 1498–1523. DOI: 10.3390/rs5041498 (see pages 18, 21, 43).
- [63] S. Kaiser, G. Grosse, J. Boike, and M. Langer. “Monitoring the transformation of arctic landscapes: Automated shoreline change detection of lakes using very high resolution imagery”. *Remote Sensing* 13:14 (2021). DOI: 10.3390/rs13142802 (see pages 18, 44).
- [64] J. P. Mondejar and A. F. Tongco. “Near infrared band of Landsat 8 as water index: a case study around Cordova and Lapu-Lapu City, Cebu, Philippines”. 29 (16 2019), pp. 1–15. DOI: <https://doi.org/10.1186/s42834-019-0016-5> (see pages 18, 22, 43).
- [65] F. Sun, W. Sun, J. Chen, and P. Gong. “Comparison and improvement of methods for identifying waterbodies in remotely sensed imagery”. *International Journal of Remote Sensing* 33:21 (2012), pp. 6854–6875. DOI: 10.1080/01431161.2012.692829 (see page 18).



- [66] J. B. Campbell and R. H. Wynne. *Introduction to Remote Sensing. Fifth Edition*. New York: Publisher: The Guilford Press, 2011 (see page 18).
- [67] Remote Sensing Phenology. *NDVI, the Foundation for Remote Sensing Phenology*. URL: <https://www.usgs.gov/special-topics/remote-sensing-phenology/science/ndvi-foundation-remote-sensing-phenology>. Accessed: 2021-12-15. 2018 (see pages 18, 20).
- [68] F. Gascon, C. Bouzinac, O. Thépaut, M. Jung, B. Francesconi, J. Louis, V. Lonjou, B. Lafrance, S. Massera, A. Gaudel-Vacaresse, F. Languille, B. Alhammoud, F. Viallefont, B. Pflug, J. Bieniarz, S. Clerc, L. Pesiot, T. Trémas, E. Cadau, R. De Bonis, C. Isola, P. Martimort, and V. Fernandez. “Copernicus Sentinel-2A Calibration and Products Validation Status”. *Remote Sensing* 9:6 (2017). DOI: 10.3390/rs9060584 (see page 19).
- [69] D. Scheffler, A. Hollstein, H. Diedrich, K. Segl, and P. Hostert. “AROSICS: An automated and robust open-source image co-registration software for multi-sensor satellite data”. *Remote Sensing* 9:7 (2017). DOI: 10.3390/rs9070676 (see page 19).
- [70] M. Benjamin. *Sentinel-2 Cloud Masking with s2cloudless*. URL: <https://github.com/benmack/eo-box.git>. Accessed: 2021-09-15. 2018 (see page 20).
- [71] F. E. Fassnacht, C. Schiller, T. Kattenborn, X. Zhao, and J. Qu. “A Landsat-based vegetation trend product of the Tibetan Plateau for the time-period 1990–2018”. *Scientific Data* 6:1 (2019), pp. 1–11. DOI: 10.1038/s41597-019-0075-9 (see page 22).
- [72] Jeffrey G. Masek. *The Landsat Program*. URL: <https://landsat.gsfc.nasa.gov/>. Accessed: 2021-10-15 (see pages 22, 23).
- [73] J. Li and D. P. Roy. “A Global Analysis of Sentinel-2A, Sentinel-2B and Landsat-8 Data Revisit Intervals and Implications for Terrestrial Monitoring”. *Remote Sensing* 9:9 (2017). DOI: 10.3390/rs9090902 (see page 22).
- [74] J. Dozier. “Spectral signature of alpine snow cover from the landsat thematic mapper”. *Remote Sensing of Environment* 28 (1989), pp. 9–22. DOI: [https://doi.org/10.1016/0034-4257\(89\)90101-6](https://doi.org/10.1016/0034-4257(89)90101-6) (see page 24).

- [75] D. K. Hall, G. A. Riggs, and V. V. Salomonson. “Development of methods for mapping global snow cover using moderate resolution imaging spectroradiometer data”. *Remote Sensing of Environment* 54:2 (1995), pp. 127–140. DOI: [https://doi.org/10.1016/0034-4257\(95\)00137-P](https://doi.org/10.1016/0034-4257(95)00137-P) (see page 24).
- [76] J. S. Deems, T. H. Painter, and D. C. Finnegan. “Lidar measurement of snow depth: A review”. *Journal of Glaciology* 59:215 (2013), pp. 467–479. DOI: 10.3189/2013JoG12J154 (see page 39).
- [77] B. Walker, E. J. Wilcox, and P. Marsh. “Accuracy assessment of late winter snow depth mapping for tundra environments using structure-from-motion photogrammetry”. *Arctic Science* 7:3 (2021), pp. 588–604. DOI: 10.1139/as-2020-0006 (see page 39).
- [78] G. E. Liston and M. Sturm. “A snow-transport model for complex terrain”. *Journal of Glaciology* 44:148 (1998), pp. 498–516. DOI: 10.3189/S0022143000002021 (see page 40).
- [79] F. Lanouette, G. Doré, D. Fortier, and C. Lemieux. “Influence of snow cover on the ground thermal regime along an embankment built on permafrost : In-situ measurements”. *68e Conférence Canadienne de Géotechnique et 7e Conférence Canadienne sur le Pergélisol, 20 au 23 septembre 2015, Québec.*: September (2015). DOI: 10.13140/RG.2.1.2482.1848 (see page 41).
- [80] M. Sturm and A. M. Wagner. “Using repeated patterns in snow distribution modeling: An Arctic example”. *Water Resources Research* 46:12 (2010). DOI: <https://doi.org/10.1029/2010WR009434> (see page 42).
- [81] S. Feng, S. Liu, L. Jing, Y. Zhu, W. Yan, B. Jiang, M. Liu, W. Lu, Y. Ning, Z. Wang, Q. Li, and J. Jia. “Quantification of the Environmental Impacts of Highway Construction Using Remote Sensing Approach”. *Remote Sensing* 13:7 (2021), p. 1340. DOI: 10.3390/rs13071340 (see page 42).
- [82] K. Herndon, R. Muench, E. Cherrington, and R. Griffin. “An assessment of surface water detection methods for water resource management in the Nigerien Sahel”. *Sensors (Switzerland)* 20:2 (2020), pp. 1–14. DOI: 10.3390/s20020431 (see page 43).

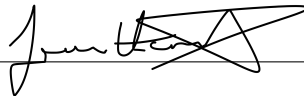
- [83] J.-M. St. Jacques and D. J. Sauchyn. “Increasing winter baseflow and mean annual streamflow from possible permafrost thawing in the Northwest Territories, Canada”. *Geophysical Research Letters* 36:1 (2009). DOI: <https://doi.org/10.1029/2008GL035822> (see page 44).
- [84] A. Runge and G. Grosse. “Comparing spectral characteristics of Landsat-8 and Sentinel-2 same-day data for arctic-boreal regions”. *Remote Sensing* 11:14 (2019), pp. 1–29. DOI: 10.3390/rs11141730 (see page 44).
- [85] Y. Du, Y. Zhang, F. Ling, Q. Wang, W. Li, and X. Li. “Water bodies’ mapping from Sentinel-2 imagery with Modified Normalized Difference Water Index at 10-m spatial resolution produced by sharpening the swir band”. *Remote Sensing* 8:4 (2016). DOI: 10.3390/rs8040354 (see page 44).
- [86] A. V. Kulkarni, J. Srinivasulu, S. S. Manjul, and P. Mathur. “Field based spectral reflectance studies to develop NDSI method for snow cover monitoring”. *Journal of the Indian Society of Remote Sensing* 30:1-2 (2002), pp. 73–80. DOI: 10.1007/BF02989978 (see page 45).
- [87] H. Zeng and G. Jia. “Impacts of snow cover on vegetation phenology in the arctic from satellite data”. *Advances in Atmospheric Sciences* 30:5 (2013), pp. 1421–1432. DOI: 10.1007/s00376-012-2173-x (see page 45).
- [88] T. C. Lantz, P. Marsh, and S. V. Kokelj. “Recent Shrub Proliferation in the Mackenzie Delta Uplands and Microclimatic Implications”. *Ecosystems* 16:1 (2013), pp. 47–59. DOI: 10.1007/s10021-012-9595-2 (see pages 46, 48).

# Selbstständigkeitserklärung

Hiermit erkläre ich, daß ich die vorliegende Arbeit selbstständig angefertigt, nicht anderweitig zu Prüfungszwecken vorgelegt und keine anderen als die angegebenen Hilfsmittel verwendet habe. Sämtliche wissentlich verwendete Textausschnitte, Zitate oder Inhalte anderer Verfasser wurden ausdrücklich als solche gekennzeichnet.

Berlin, 24.02.2022

Ort, Datum

A handwritten signature in black ink, appearing to be 'J. Müller', written over a horizontal line.

Unterschrift